

Orbital disproportionation of electronic density - a universal feature of alkali-doped fullerenes

Naoya Iwahara and Liviu F. Chibotaru

Theory of Nanomaterials Group, Katholieke Universiteit Leuven, Celestijnenlaan 200F, B-3001 Leuven, Belgium
(Dated: March 4, 2024)

Alkali-doped fullerenes A_nC_{60} show a remarkably wide range of electronic phases in function of $A = \text{Li, Na, K, Rb, Cs}$ and the degree of doping, $n = 1-5$. While the presence of strong electron correlations is well established, recent investigations give also evidence for dynamical Jahn-Teller instability in the insulating and the metallic phase of A_3C_{60} . To reveal the interplay of these interactions in fullerenes with even n , we address the electronic phase of A_4C_{60} with accurate many-body calculations within a realistic electronic model including all basic interactions extracted from first principles. We find that the Jahn-Teller instability is always realized in these materials too. More remarkably, in sharp contrast to strongly correlated A_3C_{60} , A_4C_{60} displays uncorrelated band-insulating state despite pretty similar interactions present in both fullerenes. Our results show that the Jahn-Teller instability and the accompanying orbital disproportionation of electronic density in the degenerate LUMO band is a universal feature of fullerenes.

I. INTRODUCTION

The understanding of electronic phases of alkali-doped fullerenes A_nC_{60} is a long standing and challenging task for material scientists [1]. The prominent feature of these narrow-band molecular materials is the coexistence of strong intrasite Jahn-Teller (JT) effect with strong electron correlation, which underlies the unconventional superconductivity in A_3C_{60} [2–9] and a broad variations of electronic properties in this series of materials in function of the size of alkali ions, and the degree of their doping [10–14]. External pressure and insertion of neutral spacers add new possibilities for the engineering of their electronic phases [15–17]. This was recently demonstrated for the Cs_3C_{60} fullerene, which undergoes transitions from Mott-Hubbard (MH) antiferromagnet to a high temperature superconductor ($T_c = 38$ K) and then to strongly correlated metal under external pressure [3, 4, 6–8].

Signs of JT effect in alkali-doped fullerenes were inferred from NMR [18, 19], IR [20, 21], and EELS [22, 23] spectra, and STM [24, 25] in various compounds. Recently, the parameters governing the complex JT interaction on fullerene anions have been firmly established [26–28], which opened the way for accurate theoretical investigation of the electronic states in fullerenes. It was found that in the MH insulating phase of cubic fullerenes such as Cs_3C_{60} at ambient pressure, the para dynamical JT effect is realized as independent pseudorotations of JT deformations at each C_{60} site [29]. The same para dynamical JT effect was found in the metallic phase of A_3C_{60} close to MH transition, while the pseudorotation of JT deformation at different sites are expected to be correlated with further departure from the MH transition due to the increase of the band energy [30]. These findings have found confirmation in a very recent investigation of Cs_3C_{60} fullerene, showing an almost unchanged IR spectrum on both sides in the vicinity of MH metal-insulator transition, while displaying its significant variation when the material was brought deeper into the

metallic phase [31]. Moreover, our calculations have also shown that the metallic phase in these systems exhibits an orbital disproportionation of electronic density as a result of the dynamical JT instability [30].

This successful theoretical approach is applied here for the investigation of the electronic phase in the A_4C_{60} fullerenes, containing an even number of doped electrons per site. We find that these materials exhibit a dynamical JT instability too. As in A_3C_{60} , the ground state of A_4C_{60} displays again the orbital disproportionation of electronic density, thus identifying it as a universal key feature of the electronic phases of alkali-doped fullerenes.

II. DIAGRAM OF JAHN-TELLER INSTABILITY IN A_4C_{60}

It is well established that the t_{1u} lowest unoccupied molecular orbital (LUMO) band mainly defines the electronic properties of fullerenes [1]. Following the recent treatment of A_3C_{60} [30], we consider all essential interaction in this band including the one-electron, the bielectronic and the vibronic contributions:

$$\begin{aligned} \hat{H} &= \hat{H}_t + \hat{H}_{bi} + \hat{H}_{JT}, \\ \hat{H}_t &= \sum_{\mathbf{m}, \Delta \mathbf{m}} \sum_{\lambda \lambda' \sigma} t_{\lambda \lambda'}^{\Delta \mathbf{m}} \hat{c}_{\mathbf{m} + \Delta \mathbf{m} \lambda \sigma}^\dagger \hat{c}_{\mathbf{m} \lambda' \sigma}, \\ \hat{H}_{bi} &= \frac{1}{2} \sum_{\mathbf{m}} \sum_{\lambda \sigma} [U_{\parallel} \hat{n}_{\mathbf{m} \lambda \sigma} \hat{n}_{\mathbf{m} \lambda - \sigma} \\ &+ U_{\perp} \sum_{\lambda' (\neq \lambda) \sigma'} \hat{n}_{\mathbf{m} \lambda \sigma} \hat{n}_{\mathbf{m} \lambda' \sigma'} - J \sum_{\lambda' (\neq \lambda)} (\hat{n}_{\mathbf{m} \lambda \sigma} \hat{n}_{\mathbf{m} \lambda' \sigma} \\ &- \hat{c}_{\mathbf{m} \lambda \sigma}^\dagger \hat{c}_{\mathbf{m} \lambda' \sigma} \hat{c}_{\mathbf{m} \lambda - \sigma}^\dagger \hat{c}_{\mathbf{m} \lambda' - \sigma} \\ &- \hat{c}_{\mathbf{m} \lambda \sigma}^\dagger \hat{c}_{\mathbf{m} \lambda' \sigma} \hat{c}_{\mathbf{m} \lambda' - \sigma}^\dagger \hat{c}_{\mathbf{m} \lambda - \sigma})], \end{aligned}$$

$$\hat{H}_{\text{JT}} = \sum_{\mathbf{m}} \hbar\omega \left[\sum_{\gamma} \frac{1}{2} (p_{\mathbf{m}\gamma}^2 + q_{\mathbf{m}\gamma}^2) + g \sum_{\lambda\lambda'\sigma} \sum_{\gamma} G_{\lambda\lambda'}^{\gamma} \hat{c}_{\mathbf{m}\lambda\sigma}^{\dagger} \hat{c}_{\mathbf{m}\lambda'\sigma} q_{\mathbf{m}\gamma} \right], \quad (1)$$

where, \mathbf{m} denote the fullerene sites, $\Delta\mathbf{m}$ the neighbours of site \mathbf{m} , λ, λ' the t_{1u} LUMO orbitals (x, y, z) on each C_{60} , σ, σ' the spin projections, $\hat{c}_{\mathbf{m}\lambda\sigma}$ and $\hat{c}_{\mathbf{m}\lambda\sigma}^{\dagger}$ are annihilation and creation operators of electron, respectively, $\hat{n}_{\mathbf{m}\lambda\sigma} = \hat{c}_{\mathbf{m}\lambda\sigma}^{\dagger} \hat{c}_{\mathbf{m}\lambda\sigma}$, $q_{\mathbf{m}\gamma}$ and $p_{\mathbf{m}\gamma}$ are the normal vibrational coordinate for the γ component of the h_g mode ($\gamma = \theta, \epsilon, \xi, \eta, \zeta$) and its conjugate momentum, respectively, and $G_{\lambda\lambda'}^{\gamma}$ is Clebsch-Gordan coefficient. The transfer parameters $t_{\lambda\lambda'}^{\Delta\mathbf{m}}$ of \hat{H}_t have been extracted from density functional theory (DFT) calculations (see Ref. [30] for K_3C_{60} , Supplementary Materials and Fig. 5(A) for K_4C_{60}). The frequency ω and the orbital vibronic coupling constant g for an effective single-mode JT model of C_{60}^{n-} have been calculated in Ref. [29]. The phonon dispersion was neglected because it is weak in fullerenes [1]. The projection of the bielectronic interaction in the t_{1u} LUMO band onto intrasite Hamiltonian (\hat{H}_{bi}) is an adequate approximation due to strong molecular character of fullerenes [1]. The intrasite repulsion parameters U_{\parallel} and U_{\perp} , obeying the relation $U_{\parallel} - U_{\perp} = 2J$, are strongly screened: first, by high-energy interband electron excitations reducing their value from 3 eV to ca 1 eV [32] and, second, by intra t_{1u} -band excitations. The latter can further reduce U_{\parallel} and U_{\perp} several times [32], however, the extent of this screening strongly depends on the character of the correlated t_{1u} band and can, therefore, be assessed only in a self-consistent fashion. On the other hand, the vibronic coupling to the h_g modes, representing a quadrupolar perturbation, is hardly screened. The same for the Hund's rule coupling J , for which we take the calculated molecular value [29]. We leave U_{\parallel} as the only free parameter of the theory.

The ground state has been calculated within a self-consistent Gutzwiller approach, which proved to be successful for the investigation of A_3C_{60} [30]. To unravel the role played by JT interactions in the ground electronic phase in A_4C_{60} , we first consider the case of a face centered cubic (fcc) \hat{H}_t as in A_3C_{60} , the corresponding bands being populated by four electrons per site. Figure 1(A) shows the calculated total energy as function of the amplitude q of static JT distortions of $h_g\theta$ type on fullerene sites [33, 34]. As in the case of A_3C_{60} [30], the energy curve $E_g(q)$ has two minima, one at the undistorted configuration $q = 0$ and the other at a value q_0 approximately corresponding to the equilibrium distortion in an isolated C_{60}^{4-} (see the Supplementary Materials). For U_{\parallel} smaller than the critical value $U_c \approx 0.64$ eV, the static JT distortion is quenched, $q = 0$. At $U_{\parallel} > U_c$ the JT distortion reaches its equilibrium value, q_0 . The full diagram of the total energy $E_g(q, U_{\parallel})$ is shown in Fig. 1(B).

The character of the electronic phase differs drasti-

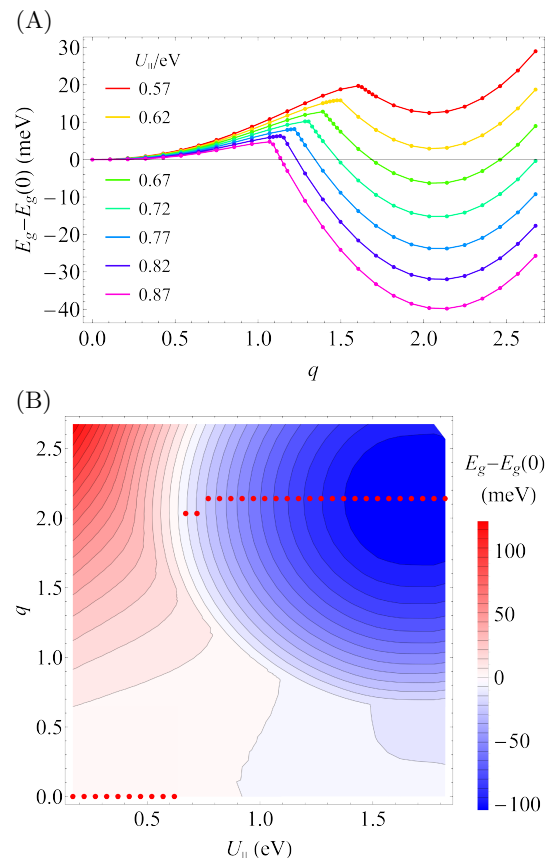


FIG. 1. (A) Total energy $E_g(q)$ of the ground electronic phase of a A_4C_{60} with cubic band dispersion (see the text) as function of amplitude of static JT distortion for several values of U_{\parallel} . (B) A two-dimensional plot of $E_g(q, U_{\parallel})$. Red and blue regions stand for positive and negative values proportional to the intensity of the color. The red points show the amplitude of spontaneous static JT distortion in function of U_{\parallel} . In both figures, the energy at $q = 0$, $E_g(0)$, is subtracted from $E_g(q)$ for each U_{\parallel} .

cally in the two domains of U_{\parallel} . The difference is clearly seen in the electron population in the LUMO orbitals n_{λ} and the Gutzwiller's reduction factor $q_{\lambda\lambda}$. The evolution of the population n_{λ} with respect to U_{\parallel} (Fig. 2(A)) shows that for $U_{\parallel} < U_c$ the phase corresponds to equally populated LUMO bands. This equally populated phase gradually becomes strongly correlated with increasing U_{\parallel} , which is testified by the accompanying decrease of the Gutzwiller's reduction factors for these bands (Fig. 2(C)). On the contrary, for $U_{\parallel} > U_c$, it exhibits orbital disproportionation of electronic density among the LUMO orbitals (Fig. 2(A)) with a sudden jump of the Gutzwiller factor (Fig. 2(C)).

The existence of the two kinds of phases with and without the JT deformation is explained by the competition between the band energy (\hat{H}_t) and the JT stabilization energy in the presence of the strong electron repulsion U_{\parallel} . The former stabilizes the system the most when the split-

ting of the orbital is absent, while the JT effect does by lowering the occupied orbitals. On the other hand, the bielectronic energy is reduced by the quenching of the charge fluctuation (localization of the electrons), which results in the decrease of the band energy and the relative enhancement of the JT stabilization. Therefore, when U_{\parallel} is small ($U_{\parallel} < U_c$), the homogeneous (with equal orbital populations) band state is favored and the JT distortion is quenched. With the increase of U_{\parallel} over U_c , the band energy is reduced to the extent that the JT stabilization on C_{60} sites is favored, resulting in orbitally disproportionated ground state.

We note that these results are general, which neither depends on the form of the JT distortion on sites nor on the uniformity of these distortions, which can also be dynamical as in A_3C_{60} [30] (*vide infra*).

III. BAND INSULATING STATE IN THE PRESENCE OF STRONG ELECTRON REPULSION

To better understand the physics of the obtained orbitally disproportionated electronic phase, first consider a simplified model for \hat{H}_t which includes only the diagonal electron transfers after orbital indices, $t_{\lambda\lambda'}^{\Delta\mathbf{m}} = \delta_{\lambda\lambda'} t_{\lambda\lambda}^{\Delta\mathbf{m}}$ (a widely used approximation for the study of multiorbital correlation effects [35–37]). Figure 3(A) shows the total energies for the two phases with and without JT distortion in function of U_{\parallel} . We see again an evolution of the ground state with the stabilization of orbitally disproportionated electronic phase in the large U_{\parallel} domain. We find this behaviour pretty similar to the case when the full \hat{H}_t for fcc lattice is considered (Fig. 3(B)). Owing to the simplification, we can fully identify the orbitally disproportionated phase because have its exact solution. Indeed, in terms of band solutions $\hat{a}_{\mathbf{k}\alpha\sigma}^{\dagger}|0\rangle = 1/\sqrt{N} \sum_{\mathbf{m}} e^{i\mathbf{k}\cdot\mathbf{m}} \hat{c}_{\mathbf{m}\alpha\sigma}^{\dagger}|0\rangle$, where N is the number of sites, we obtain for the orbitally disproportionated phase (see Supplementary Material):

$$|\Phi_0\rangle = \prod_{\mathbf{k}\sigma}^{\text{all}} \hat{a}_{\mathbf{k}x\sigma}^{\dagger} \hat{a}_{\mathbf{k}y\sigma}^{\dagger} |0\rangle, \quad (2)$$

i.e., a pure band state with occupied x and y and empty z band. In the case of a JT distortion different from the $h_g\theta$ type, the solution will be identical to Eq. (2) but involving band orbitals which are linear combinations of x , y and z orbitals. The solution Φ_0 is exact in the whole domain of U_{\parallel} . However, due to its fully disproportionated character, always corresponding to the orbital populations (2,2,0), it becomes ground state, i.e., intersects the correlated homogeneous solution (Fig. 3(A)), only under the opening of the gap between occupied degenerate orbitals x, y and the empty orbital z . This means that the orbitally disproportionated phase in Fig. 3(A) is nothing but conventional band insulator.

The obtained result is not specific to the simplified model. In the case of full \hat{H}_t (Fig. 3(B)), the orbitally disproportionated state differs only slightly from Φ_0 in Eq. (2), which is seen from the population of the orbital components of the LUMO band n_{λ} that are close to (2,2,0), Fig. 2(A), and the jump of the Gutzwiller factor to its uncorrelated value 1, Fig. 2(C). Thus, we encounter here a counterintuitive situation: with the increase of the electron repulsion on sites, the system passes from a strongly correlated metal to a uncorrelated band insulator.

To get further insight into the correlated metal to band insulator transition, we compare the electronic state of A_4C_{60} with that of the correlated A_3C_{60} which turns into MH insulator for large U_{\parallel} . In both fullerenes, the transition from the orbitally degenerate phase to the disproportionated phase is observed with the increase of U_{\parallel} , however, the nature of the latter phases is significantly different. Because orbital disproportionation is indissolubly linked to JT distortions on fullerene sites, either static or dynamic, the LUMO band in A_3C_{60} will be split in three orbital subbands. Figures 2(B) and 2(D) show that the lowest orbital subband in A_3C_{60} becomes fully occupied and practically uncorrelated ($g_{\lambda\lambda} \approx 1$) with increase of U_{\parallel} in very close analogy with the behavior of the two lowest subbands in A_4C_{60} (Fig. 2(C)). At the same time the electron correlation in the middle half-occupied subband gradually increases implying that the MH transition basically occurs in this subband [30]. Indeed, the bielectronic energy is reduced by quenching the charge fluctuations in the half-filled middle subband. This is seen as the decrease of the Gutzwiller's factor with the increase of U_{\parallel} (Fig. 2(D)), testifying about suppression of the intersite electron hopping. On the contrary, the doubly occupied orbitals are not subject to electron correlation (Gutzwiller's factor becomes close to 1, Fig. 2(D)). In the case of A_4C_{60} , the LUMO orbitals split into two doubly filled orbitals and non-degenerate empty orbital by the JT interaction (see the inset of Fig. 2(A)). The fully occupied orbitals are similar in nature to those of A_3C_{60} , being basically uncorrelated, the same for the empty orbital (all Gutzwiller's factors are close to 1, Fig. 2(C)).

IV. CONDITION FOR THE STABILIZATION OF ORBITALLY DISPROPORTIONATED PHASE

The necessary condition for achieving the band insulating state is that in the atomic limit of large U_{\parallel} , the orbitally disproportionated molecular state ($S = 0$) has lower energy than the homogeneous $S = 1$ Hund state on each C_{60} . Consider the t_{1u} orbital shell of one single fullerene site. Due to the Hund's rule coupling, the high-spin configurations ($S = 1$), e.g., (2,1,1), are stabilized by $3J$ with respect to the low-spin configurations ($S = 0$), e.g., (2,2,0). The high-spin (Hund) state always contains half-filled orbitals and leads, therefore, to MH insulator

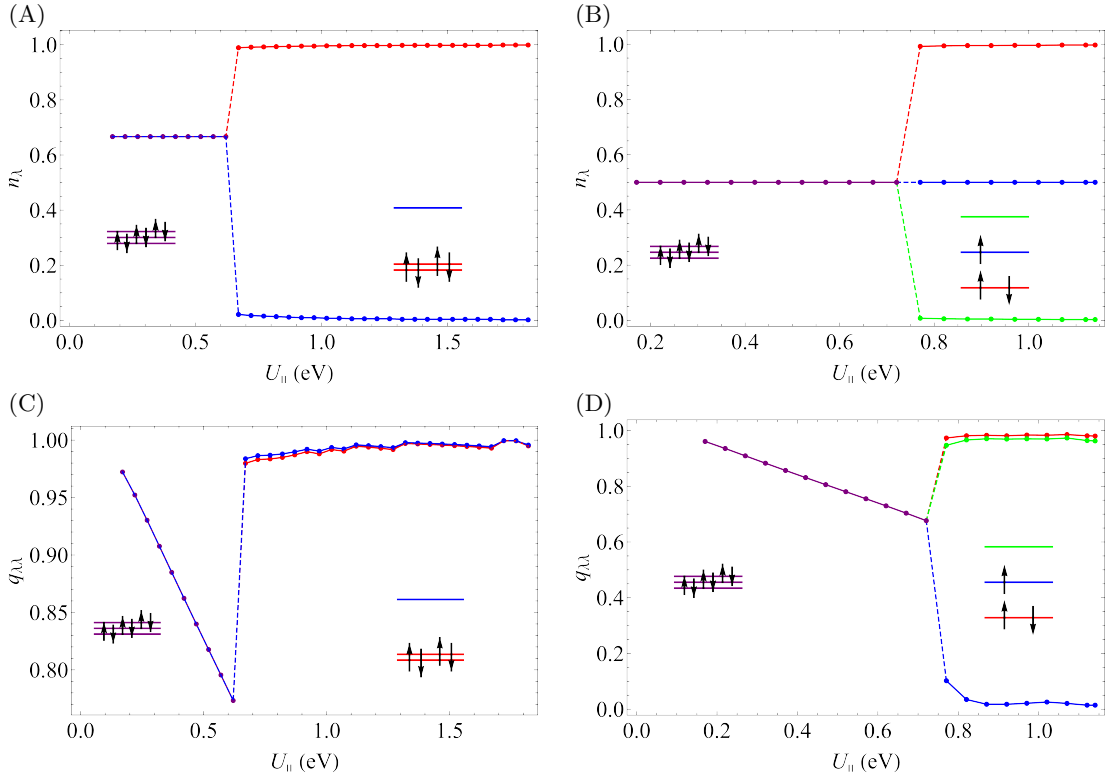


FIG. 2. (A) Occupation numbers per electron spin of LUMO orbitals n_{λ} and (C) Gutzwiller reduction factors in the corresponding bands for a model A_4C_{60} with cubic band dispersion (see the text) subject to static JT interaction as function of U_{\parallel} . (B) and (D): the same as (A) and (C), respectively, for fcc A_3C_{60} .

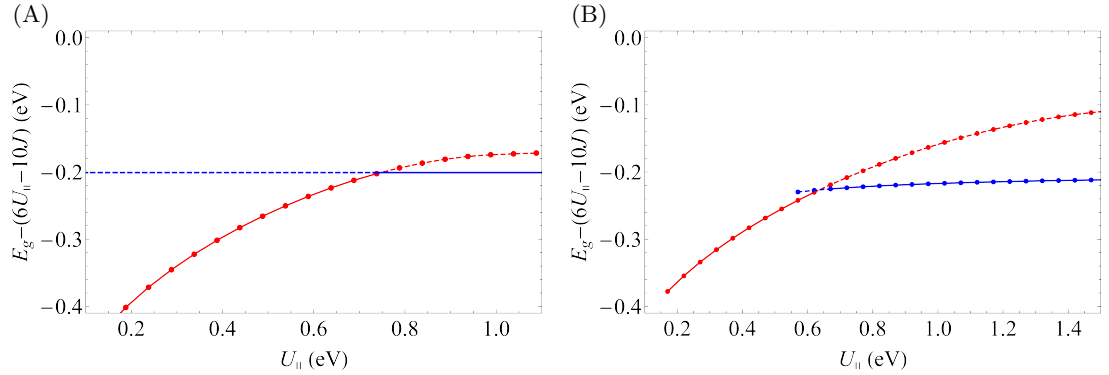


FIG. 3. (A) Total energy of the ground electronic phase of A_4C_{60} with cubic band dispersion and suppressed interband electron transfer ($t_{\lambda\lambda}^{\Delta m} = \delta_{\lambda\lambda} t_{\lambda\lambda}^{\Delta m}$) as function of U_{\parallel} . The red and the blue lines indicate the correlated band solution ($q = 0$) and band insulating solution with JT splitting, respectively, and the solid and dashed lines indicate the ground and the excited states, respectively, for each U_{\parallel} . The bielectronic energy ($6U_{\parallel} - 10J$) is subtracted from E_g . (B) The same for the model of A_4C_{60} with full transfer Hamiltonian used in Eq. (1).

in the limit of large U_{\parallel} . On the other hand, in the presence of a relatively strong static JT effect, the low-spin state is stabilized by $E_{JT} = 4E_{JT}^{(1)}$, where $E_{JT}^{(1)} = \hbar\omega g^2/2$ is the JT stabilization energy in C_{60}^- [33, 34]. Thus, the low-spin state, and, consequently, the band insulating state, is realized as the ground state when the condition

$E_{JT} > 3J$ is fulfilled. With the estimate $E_{JT}^{(1)} = 50$ meV and $J = 44$ meV [26, 29], we conclude that all A_4C_{60} with hypothetical cubic structure will be band insulators in the static JT limit at sufficiently large U_{\parallel} .

This condition is modified when there is an intrinsic orbital gap Δ_0 at fullerene sites which arises due to the

TABLE I. The criterion for correlated metal to band insulator transition in three-fold degenerate band system with four electrons per site. ^a

	Intrinsic orbital splitting	Static JTE	Dynamical JTE	Band insulator
		–	–	Never
(A)		+	–	$E_{JT} > 3J$
		+	+	$E_{JT} + \hbar\bar{\omega} > 3J$
(B)		–	–	$\Delta_0 > 3J$
		+	–	$\Delta_0 + E_{JT} > 3J$
		+	+	$\Delta_0 + E_{JT} + \frac{1}{2}\hbar\bar{\omega} > 3J$
(C)		–	–	Never
		+	–	$E_{JT} > 3J$
		+	+	$E_{JT} + \frac{1}{2}\hbar\bar{\omega} > 3J$
(D)		–	–	$(1 - \mu)\Delta_0 > 3J$
		+	–	$(1 - \mu)\Delta_0 + E_{JT} > 3J$
		+	+	$(1 - \mu)\Delta_0 + E_{JT} > 3J$

^a +/– stands for presence/absence, E_{JT} is the JT stabilization energy for C_{60}^{4-} , Δ_0 is the (non-JT) crystal-field splitting of the t_{1u} LUMO shell on one fullerene site, $\hbar\bar{\omega}/2$ is the energy gain due to the JT dynamics per dimension of the trough, and $0 \leq \mu \leq 1$. The Hund's rule energy $3J$ will be slightly modified by taking into account the multiplet structure due to the presence of two low-spin terms in C_{60}^{4-} .

lowering of the symmetry of the crystal field (CF) in non-cubic fullerenes (Table I). Band structure calculations of A_4C_{60} with body centered tetragonal (bct) lattice show that the low-symmetry CF is weak and does not admit the excited electronic states on fullerene sites. Accordingly, the strength of the JT coupling is not modified by this CF splitting. When one of the t_{1u} orbitals is destabilized by the CF splitting Δ_0 (Table I (B)), the Hund configuration (2,1,1), with $S = 1$, is also destabilized by Δ_0 , whereas the energy of the low-spin configuration (2,2,0), with $S = 0$, remains unchanged because the destabilized orbital is not populated ($n = 0$). The orbitally disproportionated state becomes the ground one when $E_{JT} + \Delta_0 > 3J$, which means that the low-symmetry CF splitting enhances the tendency toward disproportionation. Moreover, if the CF splitting Δ_0 is larger than the Hund's rule energy $3J$, the system becomes band insulator for sufficiently large $U_{||}$ even in the absence of the JT effect ($E_{JT} = 0$).

On the contrary, if two t_{1u} orbitals are equally destabilized by Δ_0 (Table I (C)), both the high-spin and the low-spin configurations are destabilized by $2\Delta_0$, thus the system does never become band insulator only due to CF splitting. The band insulator is achieved in this case only when the JT stabilization in the low-spin state is stronger than the Hund energy $3J$, which results in the same criterion as for the degenerate case (A). We stress that the amplitude of the CF splitting does not play a role in this

case. It only plays a role when the destabilizations of the low- and high-spin configurations are different, such as in the case of the second scenario (B) or the last one (D) corresponding to complete CF lift of degeneracy. In the latter case, on the argument given above, only the CF splitting between the highest two orbitals adds to the criterion, which looks now as intermediate ($0 < 1 - \mu < 1$, see Table I(D)) to the previous scenarios, (B) and (C).

According to the tight-binding simulations of the DFT LUMO band (Fig. 5(A)), the pattern of the orbital splitting for the bct K_4C_{60} corresponds to the third scenario of the CF splitting (Table I(C)) with a gap Δ_0 of ca 130 meV. Given a similar lattice structure, the same situation is expected also for Rb_4C_{60} . Therefore, according to the criterion in Table I, no band insulating state can arise in these two fullerenes, unless the JT stabilization energy exceeds the Hund energy ($3J$). Following the estimations of $E_{JT}^{(1)}$ and J (see above), we conclude that the uncorrelated band insulating phase is stabilized in A_4C_{60} with $A = K, Rb$, in agreement with experiment. In body centered orthorhombic (bco) Cs_4C_{60} , the low-symmetric CF will completely lift the degeneracy of the t_{1u} orbitals, leading to a scenario (D) in Table I. The splitting between the highest and the middle t_{1u} orbitals will enhance the tendency towards the stabilization of the band insulating state, according to the criterion in Table I.

Finally, we consider the effect of the JT dynamics on the stabilization of the orbitally disproportionated phase. In the cubic A_4C_{60} , due to a perfect disproportionation (2,2,0) of the occupation of orbital subbands, the dynamical JT effect on the fullerene sites will be unhindered by hybridization of orbitals between sites pretty much as in metallic A_3C_{60} close to MH transition [30]. The pseudorotation of JT deformations in the trough of the ground adiabatic potential surface of fullerene anion gives a gain in nuclear kinetic energy of $\hbar\bar{\omega}/2 \approx 30$ meV per dimension of the trough [29]. The gain amounts to $\hbar\bar{\omega}$ in the case of two-dimensional trough in C_{60}^{4-} [33, 34]. This will enhance the criterion for band insulator by $\hbar\bar{\omega}$ in the case of cubic lattice (Table I). For relatively large intrinsic CF gap, $\Delta_0 > \hbar\bar{\omega}/2$, one of the rotational degrees of freedom in the trough will be quenched and the JT dynamics will reduce to a one-dimensional pseudorotation of JT deformations entraining only the two degenerate orbitals in the (B) and (C) scenarios of splitting shown in Table I. This is apparently the case of bct K_4C_{60} and Rb_4C_{60} at ambient pressure. In the case of last scenario (D) of CF splitting, the JT pseudorotational dynamics will be completely quenched if the separations between the three orbitals exceed much $\hbar\bar{\omega}/2$. Whether this is the case of Cs_4C_{60} with a relevant bco lattice, remains to be answered by a DFT based analysis similar to one done here for K_4C_{60} (Figs. 5(A), (C)).

Another ingredient defining the transition from the correlated metal to band insulator is the bielectronic interaction $U_{||}$. The value of $U_{||}$ at which the band insulating state is stabilized (the crossing point of the two

phases in Fig. 3) depends on the relation between the band energy in the homogeneous correlated metal phase ($\langle \hat{H}_t \rangle$) and the gain of intrasite energy due to disproportionated orbital occupations (static and dynamic JT stabilization energies). The calculations (Fig. 3) show that in the cubic model of A_4C_{60} , the band insulating state arises already at modest values of U_{\parallel} , which means that it is always achieved in these fullerides (cf. experimental Hubbard $U \approx 0.4-0.6$ eV for K_3C_{60} [38, 39]). Since the necessary conditions for the cubic and bct A_4C_{60} are the same (Table I), the band insulating state seems to be well achieved in the bct K_4C_{60} and Rb_4C_{60} . The stabilization of the band insulating state in the bco Cs_4C_{60} seems to be facilitated by a larger U_{\parallel} expected due to the larger distance between C_{60} sites. This is in line with the experimental observation of insulating nonmagnetic state in all A_4C_{60} at ambient pressure [13, 14, 40].

We want to emphasize that the intrinsic CF splitting of the t_{1u} LUMO orbitals on C_{60} sites in fullerides does not render them automatically band insulators. Thus, the DFT calculations of K_4C_{60} (Figs. 5(A) and 5(C)) do not give a band insulator but rather a metal despite the intrinsic CF splitting of 130 meV. The same situation is realized in Cs_4C_{60} and any other fulleride in which the intrinsic CF splitting is significantly smaller than the uncorrelated bandwidth. The band insulating state (Figs. 5(B) and 5(D)) only arises due to JT distortions on fullerene sites and due to the effects of electron repulsion in the t_{1u} shell reducing much the band energy of the homogeneous metallic state.

Generalizing, the band insulating state will be achieved at any value of the gap between the highest and the middle LUMO orbitals Δ (a sum of CF and JT splittings) at C_{60} sites which fulfills the necessary condition in Table I. The only difference is that smaller Δ will require larger U_{\parallel} for achieving the intersection with the homogeneous correlated metal phase (Fig. 4). One should note that the band insulating state arises not only three-orbital systems like fullerides, but also in other orbitally degenerate systems with even numbers of electrons per site when both Δ and U_{\parallel} are sufficiently large. Thus the scenario (B) without JT effect in Table I was considered for a 1/3-filled three-orbital model with infinite-dimensional Bethe lattice [37].

V. UNIVERSALITY OF ORBITAL DISPROPORTIONATION IN FULLERIDES

Given the established orbital disproportionation of the LUMO electronic density in A_3C_{60} [29, 30], its persistence in A_4C_{60} found in the present work makes the orbital disproportionation a universal feature of electronic phases in alkali-doped fullerides. Indeed, the same electronic phase is expected also for A_2C_{60} fullerides [13, 18], which are described by essentially the same interactions as A_4C_{60} . The only difference will be the inversion of the intrinsic CF and JT orbital splittings on the fullerene

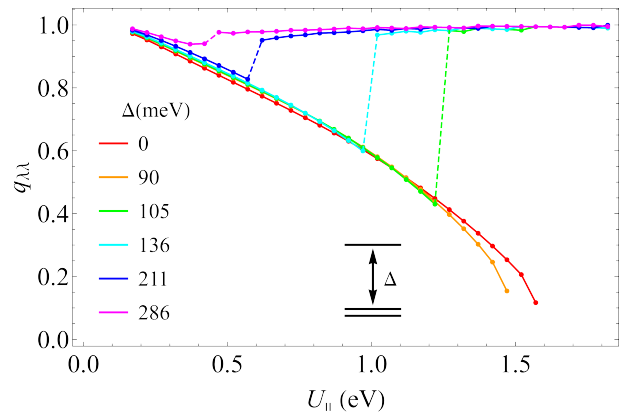


FIG. 4. Evolution of the the Gutzwiller reduction factors $q_{\lambda\lambda}$ for A_4C_{60} within the cubic model used in Fig. 1 in function of U_{\parallel} for different orbital gaps Δ , which are sums of JT and CF splittings (the former is considered arbitrary now). The monotonously decreasing line corresponds to a correlated metal, which for $\Delta < \Delta_c$ ($\Delta_c \approx 100$) evolves into a MH insulator. The jumps to $q_{\lambda\lambda} \approx 1$ for values $\Delta > \Delta_c$ correspond to onsets of band insulator.

sites.

The existence of the orbital disproportionation in fullerides is imprinted on their basic electronic properties. As discussed in Sec. III and Ref. [30], in the disproportionated phase the orbital degeneracy is lifted and the electron correlation develops in the middle subband, whereas it does not play a role in other subbands. Therefore, the MH transition also mainly develops in the middle subband [30], and hence, one has no ground whatsoever to claim strong effects of orbital degeneracy on the MH transition in these materials as was done repeatedly in the past [35, 41, 42]. Another important manifestation of the orbital disproportionation is the similar JT dynamics corresponding to independent pseudorotation of JT deformations on different fullerene sites in both MH phase [29] and strongly correlated metallic phase [30] of A_3C_{60} . This has recently found a firm experimental confirmation in the equivalence of IR spectra of the corresponding materials [31].

In A_4C_{60} , the experimental evidence for the (2,2,0) orbital disproportionated phase comes, first of all, from the observed non-magnetic insulating ground state. Moreover, as implied by the intersection picture of the two ground phases (Fig. 3), the correlated metal to band insulator transition could be observed by the decrease of the bielectronic interaction U_{\parallel} with respect to the band energy. This seems to be realized as the metal-insulator transition in Rb_4C_{60} under pressure [43], where the electron transfer (band energy) is enhanced by the decrease of the distance between the sites and U_{\parallel} is concomitantly reduced by the enhanced screening.

Further evidence for the orbitally disproportionated phase comes from spectroscopy. In the case of static JT distortions of $h_g\theta$ type on fullerene sites, the single-

particle excitations are exactly described by the uncorrelated band solutions, $|\Phi_{z\mathbf{k}\sigma}^e\rangle = \hat{a}_{z\mathbf{k}\sigma}^\dagger|\Phi_0\rangle$ for electron and $|\Phi_{\alpha\mathbf{k}\sigma}^h\rangle = \hat{a}_{\alpha\mathbf{k}\sigma}|\Phi_0\rangle$, $\alpha = x, y$, for hole quasiparticles, respectively (see the Supplementary Materials). Figure 5 shows that the dispersion of electron- and hole-like excitation basically corresponds to the decoupled z and (x, y) bands due to practically suppressed hybridization between occupied and unoccupied LUMO orbitals when the band gap opens. The hole-like excitations (Fig. 5(D)) show the density of states closely resembling the width and the shape of the LUMO feature in the photoemission spectrum [44].

VI. DISCUSSION

In this work, we investigated theoretically the ground electronic phase of A_4C_{60} fullerenes. It is found that the relatively strong electron repulsion on C_{60} sites stabilizes the uncorrelated band insulating state in these materials. A particular conclusion of the present study is that the widely used term ‘‘Jahn-Teller-Mott insulator’’ [20, 23, 45, 46] is not appropriate here because it involves

mutually excluding phenomena. A_4C_{60} or any similar multi-orbital system with even number of electrons per sites can be either a correlated metal with no JT distortions, high-spin (Hund) MH insulator, or uncorrelated band insulator stabilized by static or dynamic JT distortions. We prove here that the latter is the case in the fullerenes due to a weaker Hund’s rule interaction compared to JT stabilization energy, which is ultimately due to relatively large radius of C_{60} . Similar situation should arise in other crystals with large unit cells with local orbital degeneracy, the first candidate being the molecular crystals of K_4 clusters [47]. The present demonstration of the persistence of band insulating phase in A_nC_{60} with even n identifies the orbital disproportionation of the LUMO electronic density as a universal key feature of all alkali-doped fullerenes, which undoubtedly has a strong effect on their electronic properties. We would like to emphasize that the ultimate reason of orbital disproportionation in fullerenes is the existence of equilibrium Jahn-Teller distortions, static or dynamic, on fullerene sites. These are always present in fullerenes due to the crucial effect of electron correlation on the Jahn-Teller instability of C_{60}^{n-} sites.

-
- [1] O. Gunnarsson, *Alkali-Doped Fullerenes: Narrow-Band Solids with Unusual Properties* (World Scientific, Singapore, 2004).
- [2] O. Gunnarsson, ‘‘Superconductivity in fullerenes,’’ *Rev. Mod. Phys.* **69**, 575–606 (1997).
- [3] A. Y. Ganin, Y. Takabayashi, Y. Z. Khimyak, S. Margadonna, A. Tamai, M. J. Rosseinsky, and K. Prassides, ‘‘Bulk superconductivity at 38 K in a molecular system,’’ *Nat. Mater.* **7**, 367–371 (2008).
- [4] Y. Takabayashi, A. Y. Ganin, P. Jeglič, D. Arčon, T. Takano, Y. Iwasa, Y. Ohishi, M. Takata, N. Takeshita, K. Prassides, and M. J. Rosseinsky, ‘‘The Disorder-Free Non-BCS Superconductor Cs_3C_{60} Emerges from an Antiferromagnetic Insulator Parent State,’’ *Science* **323**, 1585–1590 (2009).
- [5] Capone, M. and Fabrizio, M. and Castellani, C. and Tosatti, E., ‘‘*Colloquium* : Modeling the unconventional superconducting properties of expanded A_3C_{60} fullerenes,’’ *Rev. Mod. Phys.* **81**, 943–958 (2009).
- [6] A. Y. Ganin, Y. Takabayashi, P. Jeglič, D. Arčon, A. Potočnik, P. J. Baker, Y. Ohishi, M. T. McDonald, M. D. Tzirakis, A. McLennan, G. R. Darling, M. Takata, M. J. Rosseinsky, and K. Prassides, ‘‘Polymorphism control of superconductivity and magnetism in Cs_3C_{60} close to the Mott transition,’’ *Nature (London)* **466**, 221–225 (2010).
- [7] Y. Ihara, H. Alloul, P. Wzietek, D. Pontiroli, M. Mazzani, and M. Riccò, ‘‘NMR Study of the Mott Transitions to Superconductivity in the Two Cs_3C_{60} Phases,’’ *Phys. Rev. Lett.* **104**, 256402 (2010).
- [8] Y. Ihara, H. Alloul, P. Wzietek, D. Pontiroli, M. Mazzani, and M. Riccò, ‘‘Spin dynamics at the Mott transition and in the metallic state of the Cs_3C_{60} superconducting phases,’’ *Europhys. Lett.* **94**, 37007 (2011).
- [9] Y. Nomura, S. Sakai, M. Capone, and R. Arita, ‘‘Exotic s -wave superconductivity in alkali-doped fullerenes,’’ *J. Phys.: Condens. Matter* **28**, 153001 (2016).
- [10] K. Tanigaki, T. W. Ebbesen, S. Saito, J. Mizuki, J. S. Tsai, Y. Kubo, and S. Kuroshima, ‘‘Superconductivity at 33 K in $Cs_xRb_yC_{60}$,’’ *Nature (London)* **352**, 222–223 (1991).
- [11] K. Tanigaki, I. Hirose, T. W. Ebbesen, J. Mizuki-Shimakawa, Y. Kubo, J. S. Tsai, and S. Kuroshima, ‘‘Superconductivity in sodium- and lithium-containing alkali-metal fullerenes,’’ *Nature (London)* **356**, 419–421 (1992).
- [12] J. Winter and H. Kuzmany, ‘‘Potassium-doped fullerene K_xC_{60} with $x = 0, 1, 2, 3, 4$, and 6 ,’’ *Solid State Commun.* **84**, 935 – 938 (1992).
- [13] D. W. Murphy, M. J. Rosseinsky, R. M. Fleming, R. Tycko, A. P. Ramirez, R. C. Haddon, T. Siegrist, G. Dabagh, J. C. Tully, and R. E. Walstedt, ‘‘Synthesis and characterization of alkali metal fullerenes: A_xC_{60} ,’’ *J. Phys. Chem. Solids* **53**, 1321 – 1332 (1992).
- [14] R. F. Kiefl, T. L. Duty, J. W. Schneider, A. MacFarlane, K. Chow, J. Elzey, P. Mendels, G. D. Morris, J. H. Brewer, E. J. Ansaldo, C. Niedermayer, D. R. Noakes, C. E. Stronach, B. Hitti, and J. E. Fischer, ‘‘Evidence for endohedral muonium in K_xC_{60} and consequences for electronic structure,’’ *Phys. Rev. Lett.* **69**, 2005–2008 (1992).
- [15] M. J. Rosseinsky, D. W. Murphy, R. M. Fleming, and O. Zhou, ‘‘Intercalation of ammonia into K_3C_{60} ,’’ *Nature (London)* **364**, 425–427 (1993).
- [16] P. Durand, G. R. Darling, Y. Dubitsky, A. Zaopo, and M. J. Rosseinsky, ‘‘The Mott-Hubbard insulating state and orbital degeneracy in the superconducting C_{60}^{3-} fullerene family,’’ *Nat. Mater.* **2**, 605–610 (2003).
- [17] A. Y. Ganin, Y. Takabayashi, C. A. Bridges, Y. Z. Khimyak, S. Margadonna, K. Prassides, and

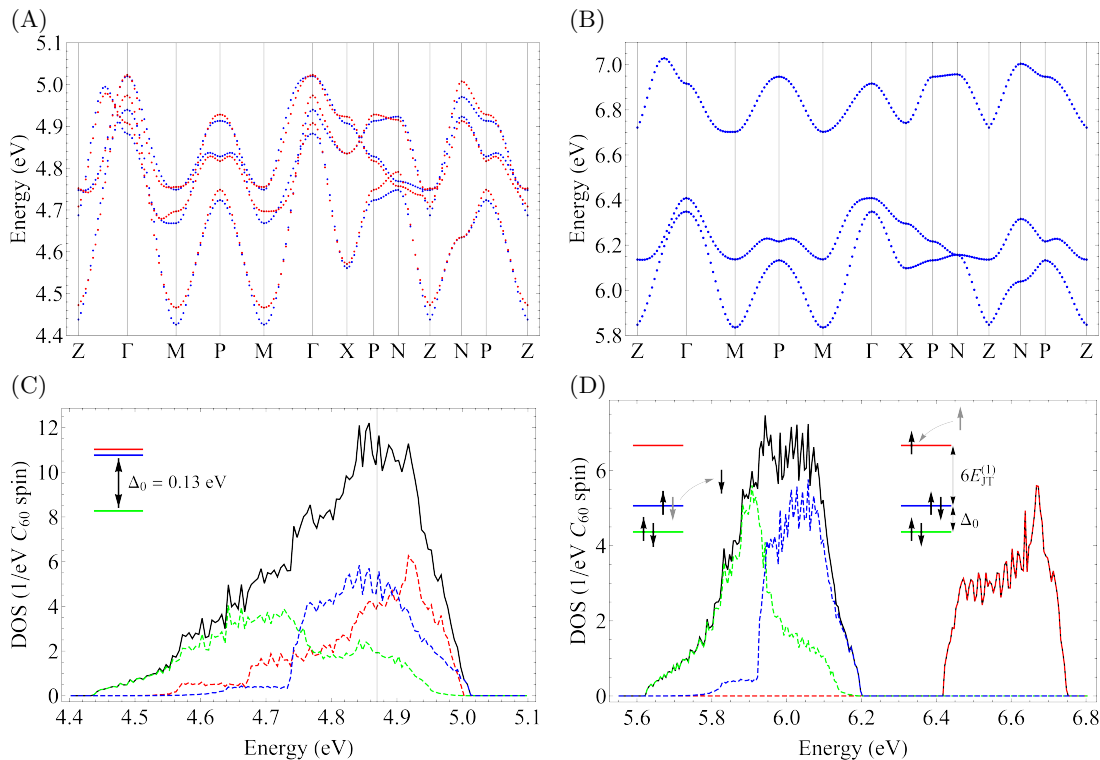


FIG. 5. (A) LUMO band dispersion and (C) corresponding density of states of K_4C_{60} calculated by DFT (GGA) for experimental structure. (B) Dispersion of single-particle excitations and (D) the corresponding density of states corresponding to the orbitally disproportionated ground state at $U_{\parallel} = 0.5$ eV and without hybridization between the occupied and empty band orbitals. The blue dots in (A) and (C) show the tight-binding simulation, and red dots in (A) the DFT calculations. The black line in (C) and (D) corresponds to a full DOS, while the colored lines the orbitally projected DOS.

- M. J. Rosseinsky, “Methylaminated Potassium Fulleride, $(CH_3NH_2)K_3C_{60}$: Towards Hyperexpanded Fulleride Lattices,” *J. Am. Chem. Soc.* **128**, 14784–14785 (2006).
- [18] V. Brouet, H. Alloul, Thien-Nga Le, S. Garaj, and L. Forró, “Role of Dynamic Jahn-Teller Distortions in Na_2C_{60} and Na_2CsC_{60} Studied by NMR,” *Phys. Rev. Lett.* **86**, 4680–4683 (2001).
- [19] A. Potočnik, A. Y. Ganin, Y. Takabayashi, M. T. McDonald, I. Heinmaa, P. Jeglič, R. Stern, M. J. Rosseinsky, K. Prassides, and D. Arčon, “Jahn-Teller orbital glass state in the expanded fcc Cs_3C_{60} fulleride,” *Chem. Sci.* **5**, 3008 (2014).
- [20] G. Klupp, K. Kamarás, N. M. Nemes, C. M. Brown, and J. Leão, “Static and dynamic Jahn-Teller effect in the alkali metal fulleride salts A_4C_{60} ($A = K, Rb, Cs$),” *Phys. Rev. B* **73**, 085415 (2006).
- [21] G. Klupp, P. Matus, K. Kamarás, A. Y. Ganin, A. McLennan, M. J. Rosseinsky, Y. Takabayashi, M. T. McDonald, and K. Prassides, “Dynamic Jahn-Teller effect in the parent insulating state of the molecular superconductor Cs_3C_{60} ,” *Nat. Commun.* **3**, 912 (2012).
- [22] M. Knupfer, J. Fink, and J. F. Armbruster, “Splitting of the electronic states near E_F in A_4C_{60} compounds ($A =$ alkali metal),” *Z. Phys. B* **101**, 57 (1996).
- [23] M. Knupfer and J. Fink, “Mott-Hubbard-like Behaviour of the Energy Gap of A_4C_{60} ($A = Na, K, Rb, Cs$) and $Na_{10}C_{60}$,” *Phys. Rev. Lett.* **79**, 2714 (1997).
- [24] A. Wachowiak, R. Yamachika, K. H. Khoo, Y. Wang, M. Grobis, D.-H. Lee, S. G. Louie, and M. F. Crommie, “Visualization of the Molecular Jahn-Teller Effect in an Insulating K_4C_{60} Monolayer,” *Science* **310**, 468–470 (2005).
- [25] J. L. Dunn, H. S. Alqannas, and A. J. Lakin, “Jahn-Teller effects and surface interactions in multiply-charged fullerene anions and the effect on scanning tunneling microscopy images,” *Chem. Phys.* **460**, 14–25 (2015).
- [26] N. Iwahara, T. Sato, K. Tanaka, and L. F. Chibotaru, “Vibronic coupling in C_{60}^- anion revisited: Derivations from photoelectron spectra and DFT calculations,” *Phys. Rev. B* **82**, 245409 (2010).
- [27] J. Laflamme Janssen, M. Côté, S. G. Louie, and M. L. Cohen, “Electron-phonon coupling in C_{60} using hybrid functionals,” *Phys. Rev. B* **81**, 073106 (2010).
- [28] C. Faber, J. Laflamme Janssen, M. Côté, E. Runge, and X. Blase, “Electron-phonon coupling in the C_{60} fullerene within the many-body GW approach,” *Phys. Rev. B* **84**, 155104 (2011).
- [29] N. Iwahara and L. F. Chibotaru, “Dynamical Jahn-Teller Effect and Antiferromagnetism in Cs_3C_{60} ,” *Phys. Rev. Lett.* **111**, 056401 (2013).
- [30] N. Iwahara and L. F. Chibotaru, “Dynamical Jahn-Teller instability in metallic fullerides,” *Phys. Rev. B* **91**, 035109 (2015).

- [31] R. H. Zadik, Y. Takabayashi, G. Klupp, R. H. Colman, A. Y. Ganin, A. Potočnik, P. Jeglič, D. Arčon, P. Matus, K. Kamarás, Y. Kasahara, Y. Iwasa, A. N. Fitch, Y. Ohishi, G. Garbarino, K. Kato, M. J. Rosseinsky, and K. Prassides, “Optimized unconventional superconductivity in a molecular Jahn-Teller metal,” *Sci. Adv.* **1**, e1500059 (2015).
- [32] Y. Nomura, K. Nakamura, and R. Arita, “*Ab initio* derivation of electronic low-energy models for C_{60} and aromatic compounds,” *Phys. Rev. B* **85**, 155452 (2012).
- [33] A. Auerbach, N. Manini, and E. Tosatti, “Electron-vibron interactions in charged fullerenes. I. Berry phases,” *Phys. Rev. B* **49**, 12998–13007 (1994).
- [34] M. C. M. O’Brien, “Vibronic energies in C_{60}^{n-} and the Jahn-Teller effect,” *Phys. Rev. B* **53**, 3775–3789 (1996).
- [35] O. Gunnarsson, E. Koch, and R. M. Martin, “Mott transition in degenerate Hubbard models: Application to doped fullerenes,” *Phys. Rev. B* **54**, R11026–R11029 (1996).
- [36] O. Gunnarsson, E. Koch, and R. M. Martin, “Mott-Hubbard insulators for systems with orbital degeneracy,” *Phys. Rev. B* **56**, 1146–1152 (1997).
- [37] T. Kita, T. Ohashi, and N. Kawakami, “Mott transition in three-orbital Hubbard model with orbital splitting,” *Phys. Rev. B* **84**, 195130 (2011).
- [38] P. A. Brühwiler, A. J. Maxwell, A. Nilsson, N. Mårtensson, and O. Gunnarsson, “Auger and photoelectron study of the Hubbard U in C_{60} , K_3C_{60} , and K_6C_{60} ,” *Phys. Rev. B* **48**, 18296–18299 (1993).
- [39] R. Macovez, M. R. C. Hunt, A. Goldoni, M. Pedio, and P. Rudolf, “Surface Hubbard U of alkali fullerenes,” *J. Elect. Spect. Rel. Phen.* **183**, 94 – 100 (2011).
- [40] M. Kosaka, K. Tanigaki, I. Hirosawa, Y. Shimakawa, S. Kuroshima, T.W. Ebbesen, J. Mizuki, and Y. Kubo, “ESR studies of K-doped C_{60} ,” *Chem. Phys. Lett.* **203**, 429 – 432 (1993).
- [41] J. P. Lu, “Metal-insulator transitions in degenerate Hubbard models and A_xC_{60} ,” *Phys. Rev. B* **49**, 5687–5690 (1994).
- [42] E. Koch, O. Gunnarsson, and R. M. Martin, “Filling dependence of the Mott transition in the degenerate Hubbard model,” *Phys. Rev. B* **60**, 15714–15720 (1999).
- [43] R. Kerkoud, P. Auban-Senzier, D. Jérôme, S. Brazovskii, I. Luk’yanchuk, N. Kirova, F. Rachdi, and C. Goze, “Insulator-metal transition in Rb_4C_{60} under pressure from ^{13}C -NMR,” *J. Phys. Chem. Solids* **57**, 143 – 152 (1996).
- [44] M. De Seta and F. Evangelisti, “LUMO band of K-doped C_{60} single phases: A photoemission and yield-spectroscopy study,” *Phys. Rev. B* **51**, 1096–1104 (1995).
- [45] M. Fabrizio and E. Tosatti, “Nonmagnetic molecular Jahn-Teller Mott insulators,” *Phys. Rev. B* **55**, 13465–13472 (1997).
- [46] V. Brouet, H. Alloul, S. Gárj, and L. Forró, “NMR Studies of Insulating, Metallic, and Superconducting Fullerenes: Importance of Correlations and JahnTeller Distortions,” in *Fullerene-Based Materials*, Struct. Bond., Vol. 109, edited by K. Prassides (Springer Berlin Heidelberg, 2004) pp. 165–199.
- [47] B. K. Rao and P. Jena, “Physics of small metal clusters: Topology, magnetism, and electronic structure,” *Phys. Rev. B* **32**, 2058–2069 (1985).

Supplemental Materials

for

“Orbital disproportionation of electronic density - a universal feature of alkali-doped fullerides”

This Supplemental Materials include:

1. Jahn-Teller effect of isolated C_{60}^{n-} ,
2. Explanation of the Gutzwiller’s approach to the Jahn-Teller system,
3. Ground state of fcc K_3C_{60} ,
4. The band structure and transfer parameters of K_4C_{60} ,
5. Band structure and DOS of K_4C_{60} with and without interorbital hybridization,
6. Eigenstates of non-hybridized system.

I. JAHN-TELLER EFFECT OF ISOLATED C_{60}^{n-}

Isolated C_{60} molecule (I_h symmetry) has triply degenerate t_{1u} LUMO level. The t_{1u} orbital couples to two nondegenerate a_g normal vibrational modes and eight five-fold degenerate h_g normal vibrational modes. In this work, we omit the a_g modes and use effective h_g mode. The Jahn-Teller (JT) Hamiltonian of C_{60}^{n-} ($n = 1 - 5$) is written as

$$H_{JT} = \sum_{\gamma} \frac{\hbar\omega}{2} (p_{\gamma}^2 + q_{\gamma}^2) + \hbar\omega g \sum_{\sigma} (\hat{c}_{x\sigma}^{\dagger}, \hat{c}_{y\sigma}^{\dagger}, \hat{c}_{z\sigma}^{\dagger}) \times \begin{pmatrix} \frac{1}{2}q_{\theta} - \frac{\sqrt{3}}{2}q_{\epsilon} & -\frac{\sqrt{3}}{2}q_{\zeta} & -\frac{\sqrt{3}}{2}q_{\eta} \\ -\frac{\sqrt{3}}{2}q_{\zeta} & \frac{1}{2}q_{\theta} + \frac{\sqrt{3}}{2}q_{\epsilon} & -\frac{\sqrt{3}}{2}q_{\xi} \\ -\frac{\sqrt{3}}{2}q_{\eta} & -\frac{\sqrt{3}}{2}q_{\xi} & -q_{\theta} \end{pmatrix} \begin{pmatrix} \hat{c}_{x\sigma} \\ \hat{c}_{y\sigma} \\ \hat{c}_{z\sigma} \end{pmatrix}, \quad (S1)$$

where ω is the frequency, g is the dimensionless vibronic coupling constant, $(q_{\theta}, q_{\epsilon}, q_{\xi}, q_{\eta}, q_{\zeta})$ are the dimensionless mass-weighted normal vibrational coordinates which transform as $2z^2 - x^2 - y^2$, $x^2 - y^2$, yz , zx , xy , respectively, under symmetric operations (for the definition of the coordinates see Fig. S1) and p_{γ} ($\gamma = \theta, \epsilon, \xi, \eta, \zeta$) is the conjugate momentum of q_{γ} . The components $\theta, \epsilon, \xi, \eta, \zeta$ of h_g mode are denoted 1,4,5,2,3, respectively, in Ref. [S1].

The h_g normal coordinates can be transformed into polar coordinates $(q, \alpha, \gamma, \theta, \phi)$ [S1]. Under appropriate rotation of the electronic coordinates $\lambda = x, y, z$,

$$\hat{c}_{l\sigma}^{\dagger} = \sum_{\lambda'=x,y,z} S_{l\lambda}(\gamma, \theta, \phi) \hat{c}_{\lambda\sigma}^{\dagger}, \quad (S2)$$

with

$$S_{l\lambda}(\gamma, \theta, \phi) = [B_P(\gamma)C_P(\theta)D_P(\phi)]_{l\lambda}, \quad (S3)$$

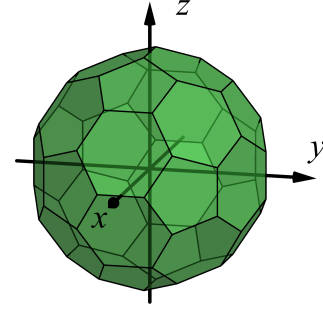


FIG. S1. Coordinate system of C_{60} .

we obtain adiabatic electronic states $l = 1, 2, 3$. Here, the rotation matrices B_P, C_P, D_P are the same as in Ref. [S1] (angle θ and the component θ of h_g coordinate are different from each other). By the unitary transformation

$$\tilde{H}_{JT} = \hat{S}^{\dagger} \hat{H}_{JT} \hat{S}, \quad (S4)$$

the potential term of the JT Hamiltonian (S1) becomes diagonal:

$$U_{JT} = \frac{\hbar\omega}{2} q^2 + \hbar\omega g q \sum_{\sigma} \left[\cos\left(\alpha + \frac{\pi}{3}\right) \hat{n}_{1\sigma} + \cos\left(\alpha - \frac{\pi}{3}\right) \hat{n}_{2\sigma} - \cos\alpha \hat{n}_{3\sigma} \right]. \quad (S5)$$

The range of α is $0 \geq \alpha < \pi/3$ or equivalent range in the configuration space.

Minimizing Eq. (S5) under the condition of $2(n_1 + n_2 + n_3) = n$, the JT deformation and the JT stabilization energy are obtained as follows [S2]. Here, n_l is an occupation number of electron ($n_l = 0, 1$). For example, when there is one electron in the LUMO orbitals (C_{60}^{-}), the amplitude of the JT coordinates at the minima of the adiabatic potential energy surface (S5) is

$$(q, \alpha) = (g, 0), \quad (S6)$$

with the occupation numbers

$$(n_1, n_2, n_3) = (0, 0, 1). \quad (S7)$$

The JT stabilization energy (the gain by the deformation) is

$$E_{JT} = E_{JT}^{(1)} = \frac{\hbar\omega g^2}{2}. \quad (S8)$$

In the case of C_{60} anion, the effective $g = 1.07$ and $\omega = 87.7$ meV, the stabilization energy $E_{JT}^{(1)} = 50.2$ meV.

By the same procedure, we obtain the JT deformations, occupations, and JT stabilization energies for all cases (Table S1).

In the strong JT coupling limit ($g \rightarrow \infty$), the ground state is well described in the space of the ground adiabatic state. Within the approximation, the kinetic term of Eq. (S4) can be separated into radial and rotational parts in the configuration space of the h_g mode [S1]. In

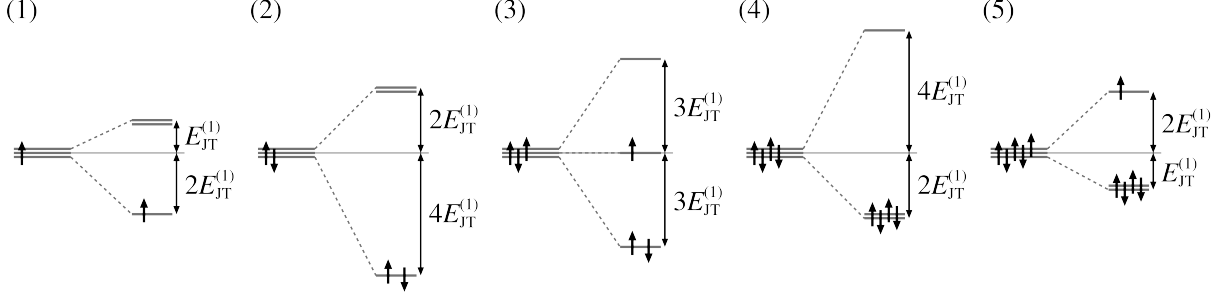


FIG. S2. JT splitting of C_{60}^{n-} . $E_{\text{JT}}^{(1)} = 50.2$ meV is the JT stabilization energy of C_{60}^- .

TABLE S1. JT distortion in polar and Cartesian coordinates, occupation numbers, and JT stabilization energies (meV) of C_{60}^{n-} . For the calculations of the Cartesian coordinates, we set the three Euler angles γ, θ, ϕ zero, leading to $q_\xi = q_\eta = q_\zeta = 0$.

n	(q, α)	(q_θ, q_ϵ)	(n_1, n_2, n_3)	E_{JT}
1	$(g, 0)$	$(g, 0)$	$(0, 0, 1)$	$E_{\text{JT}}^{(1)}$
2	$(2g, 0)$	$(2g, 0)$	$(0, 0, 2)$	$4E_{\text{JT}}^{(1)}$
3	$(\sqrt{3}g, \pi/2)$	$(0, \sqrt{3}g)$	$(2, 0, 1)$	$3E_{\text{JT}}^{(1)}$
4	$(2g, \pi)$	$(-2g, 0)$	$(2, 2, 0)$	$4E_{\text{JT}}^{(1)}$
5	(g, π)	$(-g, 0)$	$(2, 2, 1)$	$E_{\text{JT}}^{(1)}$

the case of $n = 1, 2, 4, 5$, there are three dimensional radial part and two dimensional rotational part (Eqs. (12) and (24) in Ref. [S1]): for $n = 1, 5$,

$$\begin{aligned} \tilde{H}_{\text{KE}} = & -\frac{\hbar\omega}{2} \left[\frac{1}{q^2} \frac{\partial}{\partial q} \left(q^2 \frac{\partial}{\partial q} \right) + \frac{1}{q^2 \sin \alpha} \frac{\partial}{\partial \alpha} \left(\sin \alpha \frac{\partial}{\partial \alpha} \right) \right. \\ & \left. + \frac{1}{q^2 \sin^2 \alpha} \frac{\partial^2}{\partial \gamma^2} \right] \\ & - \frac{\hbar\omega}{6q^2} \left[\frac{1}{\sin \theta} \frac{\partial}{\partial \theta} \left(\sin \theta \frac{\partial}{\partial \theta} \right) + \frac{1}{\sin^2 \theta} \frac{\partial^2}{\partial \phi^2} \right], \quad (\text{S9}) \end{aligned}$$

and for $n = 2, 4$,

$$\begin{aligned} \tilde{H}_{\text{KE}} = & -\frac{\hbar\omega}{2} \left[\frac{1}{q^2} \frac{\partial}{\partial q} \left(q^2 \frac{\partial}{\partial q} \right) + \frac{1}{q^2 \sin \alpha} \frac{\partial}{\partial \alpha} \left(\sin \alpha \frac{\partial}{\partial \alpha} \right) \right. \\ & \left. + \frac{1}{q^2 \sin^2 \alpha} \frac{\partial^2}{\partial \gamma^2} \right] + \frac{\hbar\omega}{3q^2} \\ & - \frac{\hbar\omega}{6q^2} \left[\frac{1}{\sin \theta} \frac{\partial}{\partial \theta} \left(\sin \theta \frac{\partial}{\partial \theta} \right) + \frac{1}{\sin^2 \theta} \frac{\partial^2}{\partial \phi^2} \right]. \quad (\text{S10}) \end{aligned}$$

Here, the coordinates q, α, γ are the radial coordinates and θ, ϕ are the rotational coordinates. Therefore, in the strong coupling limit, the ground state is described by the product of the radial and rotational wave functions,

$$\Psi_0 = \Phi_0^{\text{el}}(\alpha, \gamma, \theta, \phi) \phi^{\text{vib}}(q, \alpha, \gamma) \phi^{\text{rot}}(\theta, \phi), \quad (\text{S11})$$

and the ground eigen energy of \tilde{H}_{JT} is

$$E_0 = -E_{\text{JT}} + \frac{3}{2}\hbar\omega. \quad (\text{S12})$$

The first term of the right hand side is the stabilization by the static JT distortion, whereas the right hand side includes the effect of the JT dynamics. Compared with the ground energy of the five-dimensional Harmonic oscillator, $5\hbar\omega/2$, the JT dynamics stabilizes the system by $\hbar\omega$ because of the two rotational modes in the minima of the adiabatic potential energy surface.

On the other hand, when $n = 3$, there are two dimensional radial part and three dimensional rotational part (Eq. (32) in Ref. [S1]):

$$\begin{aligned} \tilde{H}_{\text{KE}} = & -\frac{\hbar\omega}{2} \left[\frac{1}{q} \frac{\partial}{\partial q} \left(q \frac{\partial}{\partial q} \right) + \frac{1}{q^2} \frac{\partial^2}{\partial \alpha^2} + \frac{9}{4q^2} \right] \\ & - \frac{\hbar\omega}{8q^2} [4\lambda_x^2 + 4\lambda_y^2 + \lambda_z^2], \quad (\text{S13}) \end{aligned}$$

where $\lambda_x, \lambda_y, \lambda_z$ are the angular momenta described by angles γ, θ, ϕ [S1]. In the ground state, the eigenstate of H_{JT} (vibronic state) is written as the product of the radial vibration around the minima and the

$$\Psi_0 = \Phi_0^{\text{el}}(\alpha, \gamma, \theta, \phi) \phi^{\text{vib}}(q, \alpha) \phi^{\text{rot}}(\gamma, \theta, \phi), \quad (\text{S14})$$

and the ground eigen energy of \tilde{H}_{JT} is

$$E_0 = -E_{\text{JT}} + \hbar\omega. \quad (\text{S15})$$

Compared with the zero vibrational energy of the five-dimensional Harmonic oscillator, there is gain by $3\hbar\omega/2$ due to the JT dynamics. In Ref. [S3], the gain by the JT dynamics is evaluated ca 90 meV for C_{60}^{3-} . On the other hand, the frequency for the effective mode is 87.7 meV, and the dynamical component of the ground energy $3\hbar\omega/2 = 132$ meV. The discrepancy is due to the intermediate strength of the orbital vibronic coupling constant g of C_{60}^{n-} anion. In the main text, we assume that, however, the relative strength of the dynamical JT stabilization is the same, and estimate the gain of C_{60}^{4-} .

II. GUTZWILLER'S APPROACH TO JAHN-TELLER SYSTEMS

A. Self-consistent Gutzwiller wave function

We briefly explain the Gutzwiller's approach to static Jahn-Teller system developed in Ref. [S4]. The

Gutzwiller's wave function Φ_G is written as

$$|\Phi_G\rangle = \hat{P}_G |\Phi_S\rangle, \quad (\text{S16})$$

where, Φ_S is a Slater determinant,

$$|\Phi_S\rangle = \prod_{\alpha\mathbf{k}\sigma}^{\text{occ.}} \hat{a}_{\alpha\mathbf{k}\sigma}^\dagger |0\rangle, \quad (\text{S17})$$

and \hat{P}_G is Gutzwiller's projector,

$$\hat{P}_G = \exp \left[-\frac{1}{2} \sum_{\mathbf{m}} \sum_{\lambda\sigma \neq \lambda'\sigma'} A_{\lambda\lambda'} \hat{n}_{\lambda\mathbf{m}\sigma} \hat{n}_{\lambda'\mathbf{m}\sigma'} \right]. \quad (\text{S18})$$

Here, we assume the translational symmetry of the system, and the state $\alpha\mathbf{k}$ is a linear combination of the localized states $\lambda\mathbf{m}$:

$$\hat{a}_{\alpha\mathbf{k}\sigma}^\dagger = \sum_{\mathbf{m}} \frac{e^{i\mathbf{k}\cdot\mathbf{m}}}{\sqrt{N}} u_{\lambda,\alpha\mathbf{k}} \hat{c}_{\lambda\mathbf{m}\sigma}^\dagger, \quad (\text{S19})$$

with orbital coefficients $u_{\lambda,\alpha\mathbf{k}}$. N is the number of sites in the system. In Eq. (S18), $A_{\lambda\lambda'}$ are real variational parameters. The Gutzwiller's variational parameter $A_{\lambda\lambda'}$ are orbital specific in order to adequately treat the split orbitals.

With the use of the Gutzwiller's wave function (S16), the ground state energy per site E_g was calculated. The latter consists of the band energy E_{band} , linear Jahn-Teller energy E_{JT} , elastic energy E_{el} , and bielectronic energy E_{bi} :

$$E_g = E_{\text{band}} + E_{\text{bi}} + E_{\text{JT}}. \quad (\text{S20})$$

The band energy is written as

$$E_{\text{band}} = \sum_{\lambda\lambda'\sigma} q_{\lambda\lambda'} \tau_{\lambda\lambda'}, \quad (\text{S21})$$

where $q_{\lambda\lambda'}$ is Gutzwiller's reduction factor, which has the meaning of quasi-particle weight [S5], and $\tau_{\lambda\lambda'}$ is the λ, λ' element of the uncorrelated band energy. For the calculation of E_{band} we used Gutzwiller's approximation [S6, S7]. The Jahn-Teller energy for C_{60}^{3-} is

$$E_{\text{JT}} = \frac{\hbar\omega}{2} q^2 - \sum_{\sigma} \frac{\sqrt{3}}{2} \hbar\omega g q (n_x - n_y), \quad (\text{S22})$$

and for C_{60}^{4-} ,

$$E_{\text{JT}} = \frac{\hbar\omega}{2} q^2 - \sum_{\sigma} \hbar\omega g q (-2n_x + n_y + n_z). \quad (\text{S23})$$

Here, we assume that the Jahn-Teller distortion (Table S1) is common to all of the fullerene sites, and q is the magnitude of the deformation. For the bielectronic energy, see Ref. [S4].

The total energy E_g contains two types of the variational parameters: orbital coefficients u (S19) and Gutzwiller's parameter A (S18). The energy E_g is minimized with respect to both u and A . Variational calculations of the energy are performed separately for u and A .

From the variation of the energy with respect to u with fixed A , we obtain Hartree-Fock like equation for each \mathbf{k} :

$$\sum_{\lambda'} h_{\lambda\lambda'}^{\mathbf{k}} u_{\lambda',\alpha\mathbf{k}} = \epsilon_{\alpha\mathbf{k}} u_{\lambda,\alpha\mathbf{k}}, \quad (\text{S24})$$

where $h_{\lambda\lambda'}^{\mathbf{k}}$ is one-electron Hamiltonian, $\epsilon_{\alpha\mathbf{k}}$ is one-electron eigen energy of the Hamiltonian. On the other hand, for fixed u , we minimize E_g with respect to A :

$$\frac{\partial E_g}{\partial A_{\lambda\lambda'}} = 0. \quad (\text{S25})$$

These two equations (S24), (S25) are solved repeatedly until we obtain the convergence of the energy. During the self-consistent calculation, the populations n_{λ} are fixed, and the ground state for each set of $\{n_{\lambda}\}$ was performed. For details of the self-consistent Gutzwiller's approach, see Ref. [S4].

B. Ground state of fcc K_3C_{60}

The ground state energy as a function of the Coulomb repulsion energy U_{\parallel} and the Jahn-Teller distortion q is shown in Fig. S3. In the figure, the ground state for each U_{\parallel} is indicated by red point. For small U_{\parallel} , the JT distortion is suppressed, whereas for $U_{\parallel} \gtrsim 0.75$ eV, the JT distortion is favored. Therefore, in the former region of U_{\parallel} , the orbitals are degenerate and equally populated in the ground state, while in the latter region, the LUMO levels are completely split and orbital disproportionation arises.

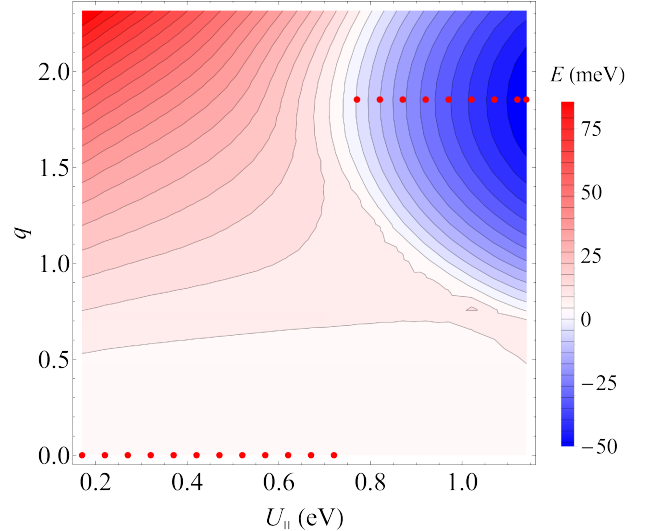


FIG. S3. Ground state energy of K_3C_{60} . The total energy is plotted as a function of the Jahn-Teller deformation q and U_{\parallel} (in meV). For each U_{\parallel} , the energy E_g at $q = 0$ is subtracted from E_g . The red points show the ground state for each U_{\parallel} .

III. TIGHT BINDING MODEL OF BCT K_4C_{60}

A. Tight binding parametrization

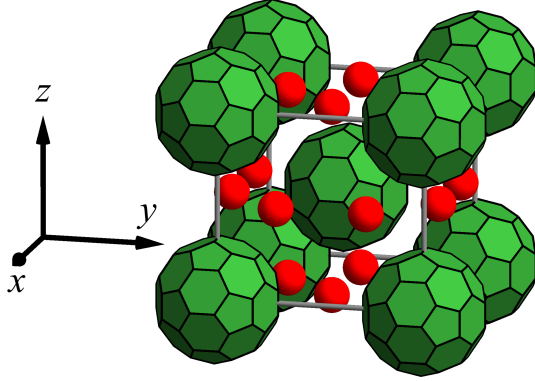


FIG. S4. Structure of bct K_4C_{60} . The green balls are fullerene C_{60} and the red spheres are K atoms which locate at $a(1/2, 0.218152, 0)$ and equivalent positions with respect to the central C_{60} .

K_4C_{60} has body centered tetragonal (bct) structure (Fig. S4). The primitive lattice vector is

$$\begin{aligned} \mathbf{a}_1 &= \frac{1}{2}(a, -a, c), & \mathbf{a}_2 &= \frac{1}{2}(a, a, c), \\ \mathbf{a}_3 &= \frac{1}{2}(-a, -a, c), \end{aligned} \quad (\text{S26})$$

where, a and c are the lattice constants. In the present work, the lattice constants were taken from the neutron diffraction data measured at 6 K ($a = 11.827 \text{ \AA}$, $c = 10.746 \text{ \AA}$) [S8]. Using $\mathbf{a}_1, \mathbf{a}_2, \mathbf{a}_3$, the nearest neighbor sites (Fig. S4) are described as

$$\Delta \mathbf{m} = \pm \mathbf{a}_1, \pm \mathbf{a}_2, \pm(-\mathbf{a}_1 + \mathbf{a}_2 + \mathbf{a}_3), \pm \mathbf{a}_3. \quad (\text{S27})$$

The next nearest neighbor sites are

$$\Delta \mathbf{m} = \pm a \mathbf{e}_x, \pm a \mathbf{e}_y, \pm c \mathbf{e}_z, \quad (\text{S28})$$

where $\mathbf{e}_x, \mathbf{e}_y, \mathbf{e}_z$ are the unit vectors along the axes x, y, z , respectively.

Because of the lower symmetry of bct lattice than fcc one, the orbital energy levels of each site split into three. Thus, the tight-binding model Hamiltonian for the bct lattice is written as the sum of the orbital energy levels part, the electron transfer part between the nearest-neighbor (nn) sites and that between next nearest neighbor (nnn) sites:

$$\hat{H}_t = \sum_{\mathbf{m}} \sum_{\lambda \sigma} \epsilon_{\lambda} \hat{n}_{\lambda \mathbf{m} \sigma} + \sum_{\mathbf{m}} \sum_{\sigma} \left(\hat{H}_{\mathbf{m} \sigma}^{\text{nn}} + \hat{H}_{\mathbf{m} \sigma}^{\text{nnn}} \right) \quad (\text{S29})$$

where the nearest neighbor term is

$$\begin{aligned} \hat{H}_{\mathbf{m} \sigma}^{\text{nn}} &= \sum_{i=1}^4 \left(t_{xx} \hat{c}_{\mathbf{m}+\Delta \mathbf{m}_i x \sigma}^{\dagger} \hat{c}_{x \mathbf{m} \sigma} + t_{yy} \hat{c}_{\mathbf{m}+\Delta \mathbf{m}_i y \sigma}^{\dagger} \hat{c}_{y \mathbf{m} \sigma} + t_{zz} \hat{c}_{\mathbf{m}+\Delta \mathbf{m}_i z \sigma}^{\dagger} \hat{c}_{z \mathbf{m} \sigma} \right) \\ &+ \sum_{(\lambda, \lambda')=(y, x), (x, y)} t_{xy} \left(-\hat{c}_{\lambda \mathbf{m}+\Delta \mathbf{m}_1 \sigma}^{\dagger} \hat{c}_{\lambda' \mathbf{m} \sigma} + \hat{c}_{\lambda \mathbf{m}+\Delta \mathbf{m}_2 \sigma}^{\dagger} \hat{c}_{\lambda' \mathbf{m} \sigma} - \hat{c}_{\lambda \mathbf{m}+\Delta \mathbf{m}_3 \sigma}^{\dagger} \hat{c}_{\lambda' \mathbf{m} \sigma} + \hat{c}_{\lambda \mathbf{m}+\Delta \mathbf{m}_4 \sigma}^{\dagger} \hat{c}_{\lambda' \mathbf{m} \sigma} \right) \\ &+ \sum_{(\lambda, \lambda')=(y, z), (z, y)} t_{yz} \left(-\hat{c}_{\lambda \mathbf{m}+\Delta \mathbf{m}_1 \sigma}^{\dagger} \hat{c}_{\lambda' \mathbf{m} \sigma} + \hat{c}_{\lambda \mathbf{m}+\Delta \mathbf{m}_2 \sigma}^{\dagger} \hat{c}_{\lambda' \mathbf{m} \sigma} + \hat{c}_{\lambda \mathbf{m}+\Delta \mathbf{m}_3 \sigma}^{\dagger} \hat{c}_{\lambda' \mathbf{m} \sigma} - \hat{c}_{\lambda \mathbf{m}+\Delta \mathbf{m}_4 \sigma}^{\dagger} \hat{c}_{\lambda' \mathbf{m} \sigma} \right) \\ &+ \sum_{(\lambda, \lambda')=(z, x), (x, z)} t_{zx} \left(\hat{c}_{\lambda \mathbf{m}+\Delta \mathbf{m}_1 \sigma}^{\dagger} \hat{c}_{\lambda' \mathbf{m} \sigma} + \hat{c}_{\lambda \mathbf{m}+\Delta \mathbf{m}_2 \sigma}^{\dagger} \hat{c}_{\lambda' \mathbf{m} \sigma} - \hat{c}_{\lambda \mathbf{m}+\Delta \mathbf{m}_3 \sigma}^{\dagger} \hat{c}_{\lambda' \mathbf{m} \sigma} - \hat{c}_{\lambda \mathbf{m}+\Delta \mathbf{m}_4 \sigma}^{\dagger} \hat{c}_{\lambda' \mathbf{m} \sigma} \right) \\ &+ \text{H.c.} \end{aligned} \quad (\text{S30})$$

and the next nearest neighbor term is

$$\begin{aligned} \hat{H}_{\mathbf{m} \sigma}^{\text{nnn}} &= t_{xx}^{\prime x} \hat{c}_{x \mathbf{m}+\mathbf{e}_x \sigma}^{\dagger} \hat{c}_{x \mathbf{m} \sigma} - t_{yy}^{\prime x} \hat{c}_{y \mathbf{m}+\mathbf{e}_x \sigma}^{\dagger} \hat{c}_{y \mathbf{m} \sigma} - t_{zz}^{\prime x} \hat{c}_{z \mathbf{m}+\mathbf{e}_x \sigma}^{\dagger} \hat{c}_{z \mathbf{m} \sigma} \\ &- t_{xx}^{\prime y} \hat{c}_{x \mathbf{m}+\mathbf{e}_y \sigma}^{\dagger} \hat{c}_{x \mathbf{m} \sigma} + t_{yy}^{\prime y} \hat{c}_{y \mathbf{m}+\mathbf{e}_y \sigma}^{\dagger} \hat{c}_{y \mathbf{m} \sigma} - t_{zz}^{\prime y} \hat{c}_{z \mathbf{m}+\mathbf{e}_y \sigma}^{\dagger} \hat{c}_{z \mathbf{m} \sigma} \\ &- t_{xx}^{\prime z} \hat{c}_{x \mathbf{m}+\mathbf{e}_z \sigma}^{\dagger} \hat{c}_{x \mathbf{m} \sigma} - t_{yy}^{\prime z} \hat{c}_{y \mathbf{m}+\mathbf{e}_z \sigma}^{\dagger} \hat{c}_{y \mathbf{m} \sigma} + t_{zz}^{\prime z} \hat{c}_{z \mathbf{m}+\mathbf{e}_z \sigma}^{\dagger} \hat{c}_{z \mathbf{m} \sigma} \\ &+ \text{H.c.} \end{aligned} \quad (\text{S31})$$

Here, ϵ_{λ} is the orbital energy level, $t_{\lambda \lambda'}$ and $t'_{\lambda \lambda'}$ are the electron transfer parameters between the nearest neigh-

bors and next nearest neighbors.

We obtained the orbital energy levels ϵ and transfer pa-

parameters t from the fitting of the DFT band structure to the tight-binding model Hamiltonian (S29), (S30), and (S31). The transfer parameters $t_{\lambda\lambda'}^m$ were taken from Ref. [S4] for fcc K_3C_{60} and derived from the DFT calculations for bct K_4C_{60} . The DFT calculations were performed within the generalized gradient approximation (GGA) with the pseudopotentials C.pbe-mt_fhi.UPF and K.pbe-mt_fhi.UPF of QUANTUM ESPRESSO 5.1 [S9]. The nuclear positions were relaxed, whereas the lattice constants from Ref. [S8] were fixed. The tight-binding parameters were obtained by fitting the DFT band to the model transfer Hamiltonian (\hat{H}_t) including the nearest neighbour and next nearest neighbour terms. The results are shown in Fig. 4(A). For the symmetric points indicated in Fig. 4(A), see Fig. S5. Table S2 shows the derived parameters. The y orbital energy level is lower than the quasidegenerate x and z orbital levels by about 130 meV. We also note that the transfer parameters to the next nearest neighbor sites t' are comparable to those of the nearest neighbor t . Particularly, the transfer parameter along the z direction t'_{xx} is the largest than the others. This is explained by the smaller distance between C_{60} sites than the other directions ($c < a$). Therefore, the electron transfer parameters to the next nearest neighbor is crucial to describe the band structure of the bct A_4C_{60} .

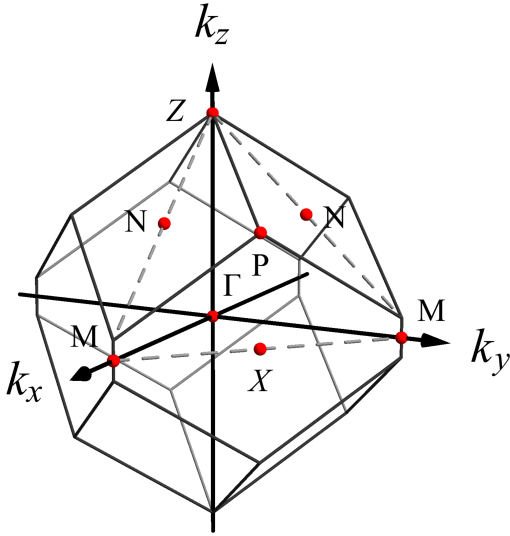


FIG. S5. The first Brillouin zone of bct lattice. The band is plotted along the path $Z = (0, 0, (1 + (a/c)^2)c/(2a)) \rightarrow \Gamma = (0, 0, 0) \rightarrow M = (1, 0, 0) \rightarrow P = (1/2, 1/2, c/(2a)) \rightarrow M = (0, 1, 0) \rightarrow \Gamma \rightarrow X = (1/2, 1/2, 0) \rightarrow P \rightarrow N = (1/2, 0, c/(2a)) \rightarrow Z \rightarrow N = (0, 1/2, c/(2a)) \rightarrow P \rightarrow Z$ in the unit of $2\pi/a$.

TABLE S2. LUMO levels (eV) and transfer parameters (meV) of bct K_4C_{60} .

ϵ_x	ϵ_y	ϵ_z	t_{xx}	t_{yy}	t_{zz}	t_{xy}	t_{yz}	t_{zx}
4.849	4.715	4.847	13.4	32.1	17.0	-17.1	14.6	0.0
t'_{xx}	t'_{yy}	t'_{zz}	t'_{xx}	t'_{yy}	t'_{zz}	t'_{xx}	t'_{yy}	t'_{zz}
14.4	7.5	-9.0	-2.6	6.1	14.8	51.3	8.8	19.8

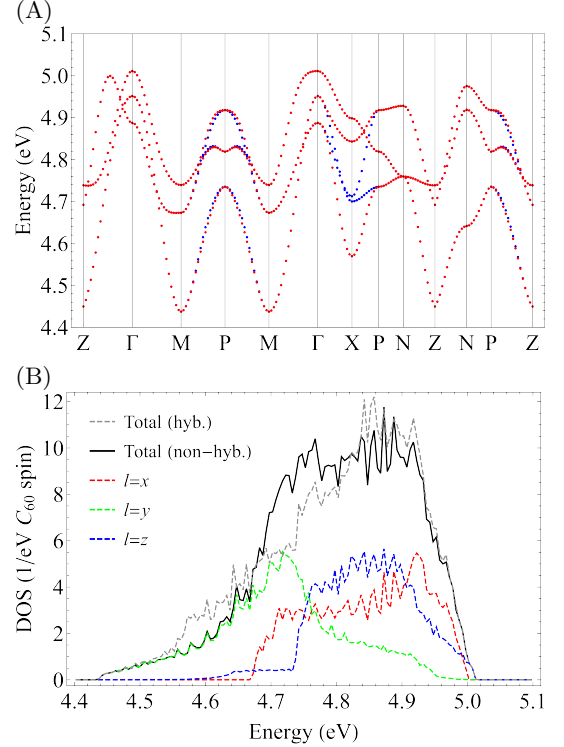


FIG. S6. (A) The band structures and (B) the density of states (DOS) of bct K_4C_{60} with and without hybridization. The Jahn-Teller splitting is not taken into account. (A) The red and blue dots indicate the presence and the absence of the hybridization between the x orbital and the other orbitals, respectively. (B) The gray dashed line is the total DOS with hybridization, the black solid line is the total DOS without hybridization, the red, green, and blue dashed lines indicate the partial DOS.

B. Effect of the hybridization of LUMO bands in bct K_4C_{60}

In bct K_4C_{60} , the effect of the interorbital hybridization is not strong. This is directly observed replacing the interorbital transfer parameter with zero. As an example, we replace the one between the x orbital and the y, z orbitals, (t_{xy}, t_{zx}). Figure S6(A) shows the hybridized (red) and non-hybridized (blue) band structures. One finds that these two bands are close to each other in almost all \mathbf{k} -points and except for around the X point (Fig. S5). By neglecting the hybridization, the split levels of

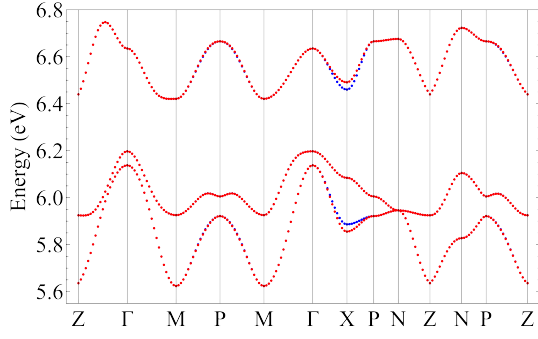


FIG. S7. The band structure with the splitting of the orbital levels. The hybridized (red) and non-hybridized (blue) band structures are similar to each other.

the hybridized band (around 4.6 eV and 4.9 eV) become quasi-degenerate (around 4.7-4.8 eV). Consequently, the total density of states (DOS) for the non-hybridized band is enhanced around the range of 4.7-4.8 eV and is reduced around 4.6 eV and 4.9 eV (Fig. S6(B)).

This hybridization effect is diminished by the splitting of the band due to the Jahn-Teller effect and Coulomb repulsion (Fig. S7). Here, we consider the Jahn-Teller distortion which would give the largest gain of the energy, i.e., x is unstabilized and y and z are stabilized, and $U_{\parallel} = 0.5$ eV. Therefore, bct K_4C_{60} can be treated as a non-hybridized band system in a good approximation.

IV. EXACT SOLUTION FOR ORBITALLY DISPROPORTIONATED STATE AND THE ONE-PARTICLE EXCITATIONS IN A_4C_{60} WITH NON-HYBRIDIZED LUMO BANDS

We show the band state and electron- and hole-quasiparticle states of non-hybridized multiband Hubbard Hamiltonian:

$$\begin{aligned} \hat{H} = & \sum_{\lambda\mathbf{k}\sigma} \epsilon_{\lambda\mathbf{k}} \hat{n}_{\lambda\mathbf{k}\sigma} + \sum_{\mathbf{m}} \left[\sum_{\lambda} U_{\parallel} \hat{n}_{\lambda\mathbf{m}\uparrow} \hat{n}_{\lambda\mathbf{m}\downarrow} \right. \\ & + (U_{\perp} - J) (\hat{n}_{1\mathbf{m}\uparrow} \hat{n}_{2\mathbf{m}\uparrow} + \hat{n}_{1\mathbf{m}\downarrow} \hat{n}_{2\mathbf{m}\downarrow}) \\ & + U_{\perp} (\hat{n}_{1\mathbf{m}\uparrow} \hat{n}_{2\mathbf{m}\downarrow} + \hat{n}_{1\mathbf{m}\downarrow} \hat{n}_{2\mathbf{m}\uparrow}) \\ & + \sum_{\lambda \neq \lambda'} J \left(\hat{c}_{\lambda\mathbf{m}\uparrow}^{\dagger} \hat{c}_{\lambda\mathbf{m}\downarrow}^{\dagger} \hat{c}_{\lambda'\mathbf{m}\downarrow} \hat{c}_{\lambda'\mathbf{m}\uparrow} \right. \\ & \left. + \hat{c}_{\lambda\mathbf{m}\uparrow}^{\dagger} \hat{c}_{\lambda'\mathbf{m}\downarrow}^{\dagger} \hat{c}_{\lambda\mathbf{m}\downarrow} \hat{c}_{\lambda'\mathbf{m}\uparrow} \right) \left. \right], \end{aligned} \quad (\text{S32})$$

where, $\epsilon_{\lambda\mathbf{k}}$ is the band energy.

For simplicity, we first consider that each site has two orbitals $\lambda = 1, 2$, then consider the case with three orbitals $\lambda = 1, 2, 3$.

We assume that the ground state of the system is band insulator type, and orbitals $\lambda = 1$ are doubly occupied and orbitals $\lambda = 2$ are empty for all \mathbf{k} . The ground state

of the Hamiltonian is given by

$$|\Phi_0\rangle = \prod_{\mathbf{k}\sigma} \hat{a}_{1\mathbf{k}\sigma}^{\dagger} |0\rangle \quad (\text{S33})$$

$$= \prod_{\mathbf{m}\sigma} \hat{c}_{1\mathbf{m}\sigma}^{\dagger} |0\rangle, \quad (\text{S34})$$

where, n is the number of electrons in the system. The ground energy E_0 is directly calculated:

$$\hat{H}|\Phi_0\rangle = \left(\sum_{\mathbf{k}} 2\epsilon_{1\mathbf{k}} + \sum_{\mathbf{m}} U_{\parallel} \right) |\Phi_0\rangle, \quad (\text{S35})$$

therefore,

$$E_0 = \sum_{\mathbf{k}} 2\epsilon_{1\mathbf{k}} + NU_{\parallel}. \quad (\text{S36})$$

Now, we add one electron to empty band orbital $2\mathbf{k}$:

$$|\Phi_{2\mathbf{k}\sigma}^e\rangle = \hat{a}_{2\mathbf{k}\sigma}^{\dagger} |\Phi_0\rangle, \quad (\text{S37})$$

This state is also an eigenstate of \hat{H} (S32):

$$\hat{H}|\Phi_{2\mathbf{k}\sigma}^e\rangle = E_{2\mathbf{k}} |\Phi_{2\mathbf{k}\sigma}^e\rangle. \quad (\text{S38})$$

Moreover, as in the previous case, Eq. (S37) is an eigenstate of each term of the Hamiltonian (electron transfer and bielectronic parts). The first part is obtained as

$$\begin{aligned} \hat{H}_t |\Phi_{2\mathbf{k}\sigma}^e\rangle &= \sum_{\lambda'\mathbf{k}'\sigma'} \epsilon_{\lambda'\mathbf{k}'} \hat{n}_{\lambda'\mathbf{k}'\sigma'} \hat{a}_{2\mathbf{k}\sigma}^{\dagger} |\Phi_0\rangle \\ &= \hat{a}_{2\mathbf{k}\sigma}^{\dagger} \sum_{\mathbf{k}'\sigma'} \epsilon_{1\mathbf{k}'} \hat{n}_{1\mathbf{k}'\sigma'} |\Phi_0\rangle + \epsilon_{2\mathbf{k}} \hat{n}_{2\mathbf{k}\sigma} \hat{a}_{2\mathbf{k}\sigma}^{\dagger} |\Phi_0\rangle \\ &= \left(\sum_{\mathbf{k}'} 2\epsilon_{1\mathbf{k}'} + \epsilon_{2\mathbf{k}} \right) |\Phi_{2\mathbf{k}\sigma}^e\rangle, \end{aligned} \quad (\text{S39})$$

where \hat{H}_t is the first term of Eq. (S32). The second part is calculated as

$$\hat{H}_{bi} |\Phi_{2\mathbf{k}\sigma}^e\rangle = \hat{a}_{2\mathbf{k}\sigma}^{\dagger} \hat{H}_{bi} |\Phi_0\rangle + [\hat{H}_{bi}, \hat{a}_{2\mathbf{k}\sigma}^{\dagger}] |\Phi_0\rangle, \quad (\text{S40})$$

where \hat{H}_{bi} is the second term of Eq. (S32). The first term is

$$\begin{aligned} \hat{a}_{2\mathbf{k}\sigma}^{\dagger} \sum_{\mathbf{m}} \sum_{\lambda} U_{\parallel} \hat{n}_{\lambda\mathbf{m}\uparrow} \hat{n}_{\lambda\mathbf{m}\downarrow} |\Phi_0\rangle &= \hat{a}_{2\mathbf{k}\sigma}^{\dagger} NU_{\parallel} |\Phi_0\rangle \\ &= NU_{\parallel} |\Phi_{2\mathbf{k}\sigma}^e\rangle. \end{aligned} \quad (\text{S41})$$

The second term is

$$\begin{aligned} [\hat{H}_{bi}, \hat{a}_{2\mathbf{k}\sigma}^{\dagger}] &= \sum_{\mathbf{m}} \frac{e^{i\mathbf{k}\cdot\mathbf{m}}}{\sqrt{N}} [\hat{H}_{bi}, \hat{c}_{2\mathbf{m}\sigma}^{\dagger}] \\ &= \sum_{\mathbf{m}} \frac{e^{i\mathbf{k}\cdot\mathbf{m}}}{\sqrt{N}} \left\{ U_{\parallel} [\hat{n}_{2\mathbf{m}\uparrow} \hat{n}_{2\mathbf{m}\downarrow}, \hat{c}_{2\mathbf{m}\sigma}^{\dagger}] \right. \\ &+ (U_{\perp} - J) \left(\delta_{\uparrow\sigma} \hat{n}_{1\mathbf{m}\uparrow} \hat{c}_{2\mathbf{m}\uparrow}^{\dagger} + \delta_{\downarrow\sigma} \hat{n}_{1\mathbf{m}\downarrow} \hat{c}_{2\mathbf{m}\downarrow}^{\dagger} \right) \\ &+ U_{\perp} \left(\delta_{\downarrow\sigma} \hat{n}_{1\mathbf{m}\uparrow} \hat{c}_{2\mathbf{m}\downarrow}^{\dagger} + \delta_{\uparrow\sigma} \hat{n}_{1\mathbf{m}\downarrow} \hat{c}_{2\mathbf{m}\uparrow}^{\dagger} \right) \\ &+ J \left(\hat{c}_{1\mathbf{m}\uparrow}^{\dagger} \hat{c}_{1\mathbf{m}\downarrow}^{\dagger} (\delta_{\sigma\downarrow} \hat{c}_{2\mathbf{m}\uparrow} - \delta_{\sigma\uparrow} \hat{c}_{2\mathbf{m}\downarrow}) \right. \\ &\left. - \delta_{\sigma\uparrow} \hat{c}_{2\mathbf{m}\downarrow}^{\dagger} \hat{c}_{1\mathbf{m}\uparrow}^{\dagger} \hat{c}_{1\mathbf{m}\downarrow} - \delta_{\sigma\downarrow} \hat{c}_{2\mathbf{m}\uparrow}^{\dagger} \hat{c}_{1\mathbf{m}\downarrow}^{\dagger} \hat{c}_{1\mathbf{m}\uparrow} \right) \left. \right\}, \end{aligned} \quad (\text{S42})$$

and thus,

$$\begin{aligned} [\hat{H}_{\text{bi}}, \hat{a}_{2\mathbf{k}\sigma}^\dagger]|\Phi_0\rangle &= \sum_{\mathbf{m}} \frac{e^{i\mathbf{k}\cdot\mathbf{m}}}{\sqrt{N}} (2U_\perp - J) \hat{c}_{2\mathbf{m}\sigma} |\Phi_0\rangle \\ &= (2U_\perp - J) |\Phi_{2\mathbf{k}\sigma}^e\rangle, \end{aligned} \quad (\text{S43})$$

where \hat{H}_{bi} is the second term of Eq. (S32). Therefore, Eq. (S37) is an eigenstate of the Hamiltonian (S32) and the eigen energy $E_{2\mathbf{k}}^e$ is

$$E_{2\mathbf{k}}^e = E_0 + \epsilon_{2\mathbf{k}} + 2U_\perp - J. \quad (\text{S44})$$

Similar situation arises when one hole is added. The state is written as

$$|\Phi_{1\mathbf{k}\sigma}^h\rangle = \hat{a}_{1\mathbf{k}\sigma} |\Phi_0\rangle \quad (\text{S45})$$

and the eigenvalue of the Hamiltonian (S32) is

$$E_{1\mathbf{k}}^h = E_0 - \epsilon_{1\mathbf{k}} - U_\parallel. \quad (\text{S46})$$

From the energies with one electron (S44) and one hole (S46), the quasi-particle band gap ΔE is obtained as:

$$\Delta E = \epsilon_{2\mathbf{k}} - \epsilon_{1\mathbf{k}'} + U_\perp - 3J. \quad (\text{S47})$$

Here, \mathbf{k} and \mathbf{k}' are the \mathbf{k} -points where the energies of the empty and the filled bands are the minimum and maximum, respectively.

Generalization of the above discussion to the cases with three or more orbitals is straight forward. In the case of three orbitals, we assume that orbitals $\lambda = 1, 2$ are doubly occupied and orbital $\lambda = 3$ is empty. The form of the eigenstates are the same as before. The eigenstate are given in the main text. The energies are

$$E_0 = \sum_{\mathbf{k}} 2(\epsilon_{1\mathbf{k}} + \epsilon_{2\mathbf{k}}) + N(2U_\parallel + 4U_\perp - 2J). \quad (\text{S48})$$

$$E_{3\mathbf{k}}^e = E_0 + \epsilon_{3\mathbf{k}} + (4U_\perp - 2J), \quad (\text{S49})$$

$$E_{\lambda\mathbf{k}}^h = E_0 - \epsilon_{\lambda\mathbf{k}} - (U_\parallel + 2U_\perp - J). \quad (\text{S50})$$

Therefore, the energy gap is

$$\Delta E = \epsilon_{3\mathbf{k}} - \epsilon_{\lambda\mathbf{k}'} + U_\perp - 3J. \quad (\text{S51})$$

Here, \mathbf{k} and $\lambda\mathbf{k}'$ are taken so that the energies of the empty and the filled bands become the minimum and maximum, respectively. These formula hold for the systems with hybridization within the occupied (or empty) bands with slight change.

-
- [S1] M. C. M. O'Brien, "Vibronic energies in C_{60}^{n-} and the Jahn-Teller effect," *Phys. Rev. B* **53**, 3775–3789 (1996).
- [S2] A. Auerbach, N. Manini, and E. Tosatti, "Electron-vibron interactions in charged fullerenes. I. Berry phases," *Phys. Rev. B* **49**, 12998–13007 (1994).
- [S3] N Iwahara and L. F. Chibotaru, "Dynamical Jahn-Teller Effect and Antiferromagnetism in Cs_3C_{60} ," *Phys. Rev. Lett.* **111**, 056401 (2013).
- [S4] N. Iwahara and L. F. Chibotaru, "Dynamical Jahn-Teller instability in metallic fullerenes," *Phys. Rev. B* **91**, 035109 (2015).
- [S5] M. C. Gutzwiller, "Correlation of Electrons in a Narrow s Band," *Phys. Rev.* **137**, A1726–A1735 (1965).
- [S6] M. C. Gutzwiller, "Effect of Correlation on the Ferromagnetism of Transition Metals," *Phys. Rev. Lett.* **10**, 159–162 (1963).
- [S7] T. Ogawa, K. Kanda, and T. Matsubara, "Gutzwiller Approximation for Antiferromagnetism in Hubbard Model," *Progress of Theoretical Physics* **53**, 614–633 (1975).
- [S8] G. Klupp, K. Kamarás, N. M. Nemes, C. M. Brown, and J. Leão, "Static and dynamic Jahn-Teller effect in the alkali metal fulleride salts $A_4\text{C}_{60}$ ($A = \text{K}, \text{Rb}, \text{Cs}$)," *Phys. Rev. B* **73**, 085415 (2006).
- [S9] P. Giannozzi *et al.*, "QUANTUM ESPRESSO: a modular and open-source software project for quantum simulations of materials," *J. Phys.: Condens. Matter* **21**, 395502 (2009).